



U.S. DEPARTMENT OF  
**ENERGY**

PNNL-18207

Prepared for the U.S. Department of Energy  
Under Contract DE-AC05-76RL01830

# **FY 2008 Infrared Photonics Final Report**

NC Anheier, Jr.  
BE Bernacki  
NA Carlie  
KL Gervais  
BK Hatchell

BR Johnson  
K Krishnaswami  
JS McCloy  
MC Phillips  
HA Qiao

December 2008



**Pacific Northwest**  
NATIONAL LABORATORY

## DISCLAIMER

This report was prepared as an account of work sponsored by an agency of the United States Government. Neither the United States Government nor any agency thereof, nor Battelle Memorial Institute, nor any of their employees, makes **any warranty, express or implied, or assumes any legal liability or responsibility for the accuracy, completeness, or usefulness of any information, apparatus, product, or process disclosed, or represents that its use would not infringe privately owned rights.** Reference herein to any specific commercial product, process, or service by trade name, trademark, manufacturer, or otherwise does not necessarily constitute or imply its endorsement, recommendation, or favoring by the United States Government or any agency thereof, or Battelle Memorial Institute. The views and opinions of authors expressed herein do not necessarily state or reflect those of the United States Government or any agency thereof.

PACIFIC NORTHWEST NATIONAL LABORATORY  
*operated by*  
BATTELLE  
*for the*  
UNITED STATES DEPARTMENT OF ENERGY  
*under Contract DE-AC05-76RL01830*

**Printed in the United States of America**

**Available to DOE and DOE contractors from the  
Office of Scientific and Technical Information,  
P.O. Box 62, Oak Ridge, TN 37831-0062;  
ph: (865) 576-8401  
fax: (865) 576-5728  
email: reports@adonis.osti.gov**

**Available to the public from the National Technical Information Service,  
U.S. Department of Commerce, 5285 Port Royal Rd., Springfield, VA 22161  
ph: (800) 553-6847  
fax: (703) 605-6900  
email: orders@ntis.fedworld.gov  
online ordering: <http://www.ntis.gov/ordering.htm>**



This document was printed on recycled paper.

(9/2003)

# **FY 2008 Infrared Photonics Final Report**

NC Anheier, Jr.	BR Johnson
BE Bernacki	K Krishnaswami
NA Carlie	JS McCloy
KL Gervais	MC Phillips
BK Hatchell	HA Qiao

December 2008

Prepared for  
the U.S. Department of Energy  
under Contract DE-AC05-76RL01830

Pacific Northwest National Laboratory  
Richland, Washington 99352



# Executive Summary

Through the duration of the NNSA Office of Nuclear Nonproliferation Research and Development (NA-22) ITAS lifecycle project, the Infrared Photonics research has been focused on developing integrated quantum cascade (QC) laser technology to enable next-generation remote sensing designs. Our team developed the concept of the integrated QC laser transmitter and originated and promoted the vision of mid-infrared (3–12  $\mu\text{m}$ ) wavelength photonics. Sustained NA-22 project funding produced the QC laser transmitter that is now deployed in follow-on projects. Our team produced nationally recognized cutting-edge research in the area of infrared transparent chalcogenide photonics. Three technical staff were recruited from outside PNNL and hired to support this research. This project also supported student research at the national laboratory, including high school, undergraduate, and graduate students. This provided a derivative benefit to NA-22, PNNL, and the educational institutions through training and mentoring next-generation students in science and technology. The student support was also the catalyst to develop research collaborations with two universities that are internationally recognized for their chalcogenide glass research.

The research conducted under this project was disseminated to the scientific community through 13 journal papers, 1 book chapter, 5 technical report publications, and 15 conference presentations listed in Appendix A. Common research themes were beneficially leveraged with other government-funded projects and the research produced leads to business growth in this area. This project was also instrumental in conceiving research topics for both university and industry SBIR NA-22 solicitations. PNNL provided technical review of the proposals generated by these solicitations, provided follow-on consultation with the principal investigators, and participated in independent project reviews.



## Acronyms and Abbreviations

APEL	Applied Process Engineering Laboratory
AR	anti-reflection
CTE	coefficient of thermal expansion
DFB	distributed feedback
DTA/TGA	differential thermal analysis and thermo gravimetric analysis
EDM	electrical discharge machining
EDS	energy dispersive spectroscopy
FP	Fabry-Perot
FTIR	Fourier transform infrared
FWHM	Full Width at Half Maximum
GaP	gallium phosphide
Ge	germanium
HHL	high heat load
ITAS	Infrared Technology for Advanced Sensors
MCT	mercury-cadmium telluride
MCZT	mercury-cadmium-zinc-telluride
NA	numerical aperture
NA-22	NNSA Office of Nuclear Nonproliferation Research and Development
NNSA	National Nuclear Security Administration
NOMSL	Non-Oxide Materials Synthesis Laboratory
OD	outer diameter
OFHC	oxygen-free, high-conductivity copper
PNNL	Pacific Northwest National Laboratory
QC	quantum cascade
RIU	refractive index units
RMS	root mean square
SBIR	small business innovation research
SEM	scanning electron microscopy
TE	transverse electric
TEC	thermoelectric cooler
TM	transverse magnetic
UV	ultraviolet
WFE	wavefront error
XRD	x-ray diffraction



# Contents

Executive Summary .....	v
Acronyms and Abbreviations.....	vii
1.0 Introduction.....	1.1
2.0 ITAS Infrared Photonics Lifecycle – Research Highlights and Capabilities .....	2.1
3.0 Chalcogenide Glass Thin Film Deposition.....	3.1
3.1 Cleanroom Facility Update .....	3.1
3.2 Film Adhesion and Delamination Investigation.....	3.1
3.3 Film Characterization .....	3.5
4.0 Lens Design for QC Laser High Heat Load Package and Waveguide Coupling .....	4.1
4.1 Preliminary Considerations .....	4.1
4.2 0.85 Collimating Lens .....	4.1
4.3 0.85 NA Lens Testing Results.....	4.3
4.4 0.85 NA Collimating Lens Optimized at 5 $\mu\text{m}$ .....	4.4
4.5 0.85 NA Collimating Lens Optimized at 5 $\mu\text{m}$ Test Results .....	4.5
4.6 0.6 NA Fiber/Waveguide Coupling Lens.....	4.5
5.0 QC Laser Transmitter Integration.....	5.1
5.1 Design Goals, Approach, and Specifications .....	5.1
5.2 Packaging and Collimation Investigation .....	5.1
5.3 HHL QC Laser Transmitter Design Update.....	5.5
5.4 HHL Package Thermal Modeling .....	5.6
6.0 Chalcogenide Optical Fiber Research .....	6.1
6.1 Fiber Jacket Removal .....	6.1
6.2 Fiber Cleaving Investigation .....	6.2
6.3 Fiber Polishing Investigation .....	6.3
6.4 Fiber Optical Characterization .....	6.4
7.0 Advanced Chalcogenide Photonic Components.....	7.1
7.1 Basic Waveguide Structure .....	7.1
7.2 Y-Junction Beam Combiner Design and Modeling .....	7.3
7.3 Device Fabrication and Testing.....	7.4
8.0 Mid-Infrared Refractive Index Measurement of Chalcogenide Glass Materials Using Prism Coupling .....	8.1
8.1 Prism Coupler Method .....	8.1
8.2 Mid-Infrared Apparatus.....	8.2

8.3 Mid-Infrared Index Measurements.....	8.4
8.4 Photomodification Studies .....	8.6
9.0 Summary.....	9.1
10.0 References.....	10.1
Appendix A Papers and Presentations Generated by This Project .....	A.1

# Figures

3.1	CaF <sub>2</sub> and SU-8 Transmission Spectrum in the Visible and Mid-Infrared Wavelength.....	3.2
3.2a	Sections Across a Film and Substrate Interface were Chosen to Extract Atomic Percentage Data.....	3.4
3.2b	Atomic Percentage of Elements in a Sample with a 1- $\mu$ m-thick CaF <sub>2</sub> Layer .....	3.4
3.2c	Atomic Percentage of Elements in a Sample on a Si Substrate.....	3.4
3.2d	Atomic Percentage of Elements in a Sample with a 2- $\mu$ m-thick SiO <sub>2</sub> Layer.....	3.4
3.3	XRD Spectrum of Unannealed and Annealed As <sub>2</sub> S <sub>3</sub> Film Using Different Annealing Parameters .....	3.5
3.4	Refractive Indices of Unannealed, Annealed As <sub>2</sub> S <sub>3</sub> Films and Bulk Material.....	3.6
4.1	Layout Drawing Showing the Final Design for the Meniscus-Shaped Germanium Collimating Lens .....	4.2
4.2	Plot of Strehl Ratio versus Lens Translation from its Optimum On-Axis Position .....	4.3
4.3	Bar Chart Showing the Measured RMS WFE Values for the Twenty-Six 0.85 NA Germanium Collimating Lenses Designed Expressly for the HHL Package Requirements.....	4.3
4.4	Change in RMS WFE as a Function of Element Decenter.....	4.4
4.5	Value of Strehl Ratio for Each Lens Tested for the HHL Collimating Lens Optimized for Use at 5 $\mu$ m.....	4.5
4.6	Optical Layout Showing the 0.6 NA Lens at Focus.....	4.7
4.7	Plot of Strehl Ratio versus Element Decenter for the 0.6 NA Germanium Fiber Coupling Lens .....	4.7
5.1	DFB QC Laser C-mount in a HHL Package .....	5.2
5.2	(a) Emission Wavelength verses Temperature at a Fixed Injection Current, and (b) Emission Wavelength verses Injection Current at a Fixed Temperature.....	5.3
5.3	(a) FTIR Spectra Showing Multimode Behavior without Collimation Lens Installed, and (b) FTIR Spectra Suggesting Single-Mode Behavior with Collimation Lens Installed.....	5.3
5.4	(a) Wavelength Drift over 90 Hours, and (b) A 1°C Room Temperature Variation Produced Nominally 1.3 ppm Peak-to-Peak Wavelength Shift .....	5.4
5.5	(a) HITRAN 2004 Water Spectrum within the DFB QC Laser Tuning Range; (b) Direct Transmission Trace of the Strong Water Line.....	5.4
5.6	(a) Submount Component with Micro-Finished Surface; (b) Zero Radius Machined Mating Corner .....	5.6
5.7	(a) Exploded and (b) Assembled HHL QC Laser Transmitter with Hamamatsu QC Laser Submount.....	5.7
5.8	(a) Component Configuration Used in the Thermal Simulation; (b) Critical Thermal Contact Surfaces.....	5.8
5.9	Temperature Distribution from Thermal Simulations.....	5.8
6.1	Images of the Cleaved Facet When Fiber Tension was ~100 psi, <60 psi, and 60 psi with Metal Bar Installed .....	6.2
6.2	Images of Angle Cleaved Surfaces: Top View and Side View Obtained by Using Fiber Tension of 80 psi and the Metal Bar .....	6.3

6.3	Fiber Facet after Polishing with 12 $\mu\text{m}$ , 9 $\mu\text{m}$ , 3 $\mu\text{m}$ , 1 $\mu\text{m}$ , and 0.3 $\mu\text{m}$ Grits.....	6.4
6.4	Experimental Apparatus to Measure the Emission Profile of Mid-Infrared Beam from a Single Mode Chalcogenide Fiber Optic Cable.....	6.5
6.5	(a) Magnified Image of the Fiber Facet Showing Emission from the Core Along with Light Leaking from the Cladding due to the Presence of Cladding Modes; (b) Beam Profiles in Pixel Dimensions along the X and Y Directions Showing the Presence of Cladding Modes.....	6.6
6.6	(a) Magnified Image of the Fiber Facet of a Gallium-Coated Fiber, Showing Emission Only from the Core and None from the Cladding; (b) Beam Profiles in Pixel Dimensions Along the X and Y Directions Showing that the Gallium Coatings Quenched the Cladding Modes.....	6.6
6.7	Emission from the Output Facet of the Chalcogenide Fiber Demonstrating near Gaussian Profiles in Both X and Y Directions, Indicative of a Single-Mode Emission.....	6.7
6.8	Modeled Data Shown Plotted with the Measured Far-Field Divergence Data, Revealing a Good Fit for the Model Assumptions Shown in the Above Table.....	6.8
6.9	Image of the Mode Field Shown Earlier Plotted with Its Gaussian Fit.....	6.9
6.10	Model Data of the Mode Profile for the Chalcogenide Fiber Shown Compared with the Experimental Data Shown Earlier.....	6.9
7.1	(a) Contour Map Depicts the Index Distribution for the Photomodified Waveguide Employing Chalcogenide Glasses for 5 $\mu\text{m}$ Operation; (b) Cross-sectional View along the Y-Axis Shows the Mode Structure and Its Penetration into the Cladding and Capping Layers of the Y-Junction Waveguide Structure.....	7.1
7.2	Computed Mode Spectrum for the Waveguide Optimized to Operate at $\lambda= 5 \mu\text{m}$ Showing Single-Mode Operation.....	7.2
7.3	Evolution of the Launch Beam in the Waveguide Described Above and the Output of Two Monitors.....	7.2
7.4	Final Y-Junction Waveguide Beam Combiner Consisting of Two S-bends and One Straight Section.....	7.3
7.5	Coordinate System Used to Fabricate the Y-Junction Beam Combiner Described in the Text.....	7.4
7.6	(a) Laser Current Ramp Waveform; (b) Detected Laser Output Intensity.....	7.5
7.7	Transmission Measured Through Solid Ge Etalon with Free Spectral Range of 0.0475 $\text{cm}^{-1}$ .....	7.6
7.8	Transmission Measured Through Waveguide Written with 1-mW Power, Normalized to the Input Laser Intensity for TE and TM Polarization.....	7.6
7.9	Position of WG Transmission FP Fringes and Linear Fit Used to Determine $N_{\text{eff}}$ .....	7.7
7.10	Measured Group Refractive Index and Waveguide Loss Versus Writing Laser Dose for TE and TM Polarization.....	7.8
7.11	Calculated Group Refractive Index and Waveguide Effective Index Versus Photoinduced Index Change of the Waveguide Core for TE and TM Modes.....	7.9
8.1	Metricon Model 2010 Prism Coupler Arrangement.....	8.1
8.2	Simulated Output Intensity as a Function of Incident Angle for Bulk Samples and Thin Films.....	8.2
8.3	Optical Configuration of the Prism Coupler System, Modified for Operation in the Mid-Infrared Spectral Region.....	8.3

8.4	Measured Refractive Index Dispersion of Bulk AMTIR2, Compared with Reference Data for AMI, and Index Dispersions for As-Deposited and Annealed Films .....	8.5
8.5	Refractive Index Data of the As <sub>2</sub> Se <sub>3</sub> Film Measured Between 3.3 to 10.6 μm as a Function of Dose.....	8.6
8.6	Refractive Index of the As <sub>2</sub> Se <sub>3</sub> Film at 1.547 and 5.348 μm as a Function of Dose.....	8.7
8.7	Refractive Index Data of the Annealed Film as a Function of Laser Dose .....	8.8

## Tables

4.1	Design Summary for the 0.85 NA Germanium Collimating Lens .....	4.2
4.2	Design Summary for the 0.85 NA HHL Collimating Lens that was Optimized for Use at a Wavelength of 5 μm .....	4.4
4.3	Design Summary for the 0.6 NA Fiber/Waveguide/Collimator Lens .....	4.6
7.1	Device Parameters for the Original Waveguide Design and the New Design Optimized for Use at λ = 5.0 μm .....	7.1



## 1.0 Introduction

During FY 2008, Pacific Northwest National Laboratory's (PNNL's) Infrared Photonics research team continued developing infrared photonics capabilities in response to the demand for lighter, more compact, and integrated remote sensing system designs. In this report we provide the lifecycle project highlights and a summary of the FY 2008 research progress for the Infrared Photonics project (a subtask under the ITAS program [PL211i]). Detailed background information on PNNL's chalcogenide infrared photonics research can be found in our previous reports (Anheier et al. 2004; Anheier et al. 2005; Anheier et al. 2006; Anheier et al. 2007).

In Section 2, we discuss the tangible staff contributions, significant research results, and the laboratory capabilities created as consequences of the NA-22 project funding. In Section 3, we provide an update of our thin film deposition cleanroom and the results of our film adhesion and film characterization study. In Section 4, we report on design and measured performance of QC laser and waveguide coupling lenses. Section 5 presents an update on the QC laser transmitter integration and laser performance. Section 6 presents our chalcogenide optical fiber processing investigation. Section 7 provides a progress update on the advance chalcogenide photonic component design, fabrication, and evaluation. Section 8 provides an introduction to our mid-infrared index measurements of chalcogenide glass. Finally, Section 9 provides a summary of our efforts in FY 2008 within the Infrared Photonics project.



## 2.0 ITAS Infrared Photonics Lifecycle – Research Highlights and Capabilities

PNNL has developed unique expertise and capabilities in the area of infrared photonics with primary applications in chemical sensing aimed at the NA-22 nuclear nonproliferation mission. To fulfill our project objective, PNNL has created innovative infrared technologies by developing and maturing designs and methods to produce compact and efficient infrared photonic components. These components now play an important role in infrared remote sensing, enabling the development of novel optical sensor designs and techniques.

To support this research, significant investments were made in both laboratory improvements and equipment acquisition to enable this research effort to achieve our goals and resolve the technological challenges needed to support the NA-22 mission. Within these research laboratories, thin films of chalcogenide glass were deposited onto silicon wafers and subsequently fabricated into planar waveguides (Ho et al. 2006), splitters, and couplers for mid-infrared applications using direct-laser writing. These devices were designed using RSoft's BeamPROP™ and FullWAVE™ software packages. To establish repeatable process parameters, the deposited thin films were fully characterized for their material and optical properties. Thin film optical constants were derived from the measured absorption spectra, while the change in refractive index due to the laser writing was measured using a custom-built lateral shearing interferometer (Krishnaswami et al. 2008c). The material properties of these thin films were measured using a scanning electron microscope (SEM) equipped with an electron dispersive spectrometer (EDS), which provided structural detail and chemical composition. X-ray diffraction (XRD) was used to verify the amorphous/crystalline nature of both pre- and post-annealed thin films (Allen et al. 2006).

Because metrology tools in the mid-infrared are not commercially available, PNNL invested a portion of its resources to develop mid-infrared metrology tools needed to characterize the performance of mid-infrared photonic components and systems. PNNL has recently developed a prism coupler that permits the measurement of absolute refractive index in chalcogenide glasses at mid-infrared wavelengths (Carlie et al. 2008). Also developed was a Twyman-Green mid-infrared interferometer used to collect and analyze wavefront data from PNNL-designed mid-infrared aspheric lenses (Bernacki et al. 2008a). Lens designs developed by PNNL, then fabricated using single-point diamond turning methods, were subsequently verified to have diffraction-limited optical performance using this interferometer. A dedicated test apparatus was constructed to measure divergence and emission profiles from mid-infrared quantum cascade lasers and chalcogenide optical fibers. Using this apparatus, PNNL produced the first experimental measurement data for intrinsic beam propagation metric ( $M^2$ ) and astigmatism for QC lasers (Krishnaswami et al. 2008a). PNNL also developed the necessary technology and methods to process chalcogenide optical fibers including cleaving, polishing, tapering, and fusing. Chalcogenide fibers were processed using a Vytran large-core fiber splicer at low temperatures, providing the capability to fabricate mid-infrared fiber optic components. Our group has also developed compression-molding expertise that provided the ability to produce miniature chalcogenide glass optical elements.

Included as part of the Infrared Photonics research are staff and facilities at PNNL's Applied Process Engineering Laboratory (APEL). The APEL facility has over 6,000 square feet of laboratory space committed to glass science research. APEL's capabilities extend from compositional design of glasses to

meet specified design criteria (durability, viscosity, crystallinity, thermal expansion, chemical compatibility, color, etc.) to glass synthesis, sample preparation, and characterization. The lab is equipped with over 20 high-temperature furnaces, 12 low-temperature-drying ovens, and 12 fume hoods. The characterization tools include simultaneous differential thermal analysis and thermo gravimetric analysis (DTA/TGA), high-temperature viscometer, dilatometry, and optical microscopy. An additional 1000 square feet of lab space is dedicated to the Non-Oxide Materials Synthesis Laboratory (NOMSL) used to fabricate chalcogenide, chalcopyrite and other photonic, electronic, and magnetic materials. This facility is capable of synthesizing and purifying materials under completely anoxic and anhydrous conditions using a combination of atmospherically controlled glove box and ultra-high vacuum glass sealing technology. High-purity fused quartz ampoules can be loaded with stoichiometric quantities of the desired elements, evacuated, sealed and thermally processed without ever exposing the elements to atmosphere. Dedicated chambers and processes have been developed that can be used for both purifying and/or thin-film deposition of chalcogenide glasses. Microstructural and microchemical characterization of these glasses is accomplished via optical microscopy and SEM/EDS and XRD.

In summary, the mid-infrared capabilities and expertise developed under this NA-22 funded project include enhanced laboratory research space and equipment, chalcogenide glass processing, QC laser expertise, waveguide design and fabrication, lens design and fabrication, fiber optic processing, sensor design and integration, and new infrared metrology tools. The research conducted under this project further strengthens PNNL's leadership position in the area of nonproliferation technology development.

## 3.0 Chalcogenide Glass Thin Film Deposition

### 3.1 Cleanroom Facility Update

The maintenance of a cleanroom facility remains a critical component for the continued production of chalcogenide glass thin films. The capability has been expanded to include an ion gun chamber for substrate cleaning prior to deposition, a three-gun magnetron sputtering system for various metal and dielectric thin film deposition, a programmable digital vacuum annealing oven, and a broad beam ultraviolet (UV) lamp at 366-nm wavelength for photolithography. A quartz lamp was installed inside the chalcogenide thin film deposition chamber to provide in-situ baking to dehydrate the substrates prior to deposition.

### 3.2 Film Adhesion and Delamination Investigation

Silicon wafers with a silicon oxide layer were selected as substrates for chalcogenide glass films in our past research because the low refractive index  $\text{SiO}_2$  acted as a barrier layer to prevent evanescent coupling into the high refractive index silicon wafer. The next generation of this device omitted the  $\text{SiO}_2$  layer from our bi-layer chalcogenide film structure (3.8- $\mu\text{m}$   $\text{As}_2\text{Se}_3$  on the top of 4.5- $\mu\text{m}$   $\text{As}_2\text{S}_3$ ) after a beam propagation simulation using the Beam-PROP<sup>TM</sup> software confirmed that a 4.5- $\mu\text{m}$ -thick  $\text{As}_2\text{S}_3$  cladding layer was sufficient to confine light within the  $\text{As}_2\text{Se}_3$  core. After consistently experiencing glass film delamination on silicon substrates, we identified substrate surface cleanliness, monolayer water and mismatch in thermal expansion coefficients as main causes of film adhesion failure and delamination. Among these three, the coefficient of thermal expansion mismatch is a primary contributor of the adhesion failure. This was demonstrated through the successful deposition and annealing of 8.3- $\mu\text{m}$ -thick bi-layer chalcogenide glass films on  $\text{CaF}_2$  substrates which have a coefficient of thermal expansion (CTE) of  $\sim 19 \times 10^{-6}/^\circ\text{C}$  compared to chalcogenide glass films that have a CTE of  $\sim 21 \times 10^{-6}/^\circ\text{C}$ . Silicon, on the other hand, has a CTE of  $3.42 \times 10^{-6}/^\circ\text{C}$ , which is significantly different compared to chalcogenide glass. In addition,  $\text{CaF}_2$  also demonstrates greater than 90% transmission up to 8  $\mu\text{m}$ , as shown in Figure 3.1.

Based on the above observations, we proceeded to identify a source for  $\text{CaF}_2$  substrates but eventually found that  $\text{CaF}_2$  substrates were not widely available and therefore they were expensive. Furthermore, the production of  $\text{CaF}_2$  wafers had a very low yield, further exacerbating the problem, with poor surface finish compared to silicon wafers. Polycrystalline  $\text{CaF}_2$  substrates were not considered as a viable substrate because they could not be cleaved. To combine the high thermal expansion property of  $\text{CaF}_2$  with optical quality and cleavability of silicon, we investigated the possibility of depositing  $\text{CaF}_2$  films onto silicon substrates.

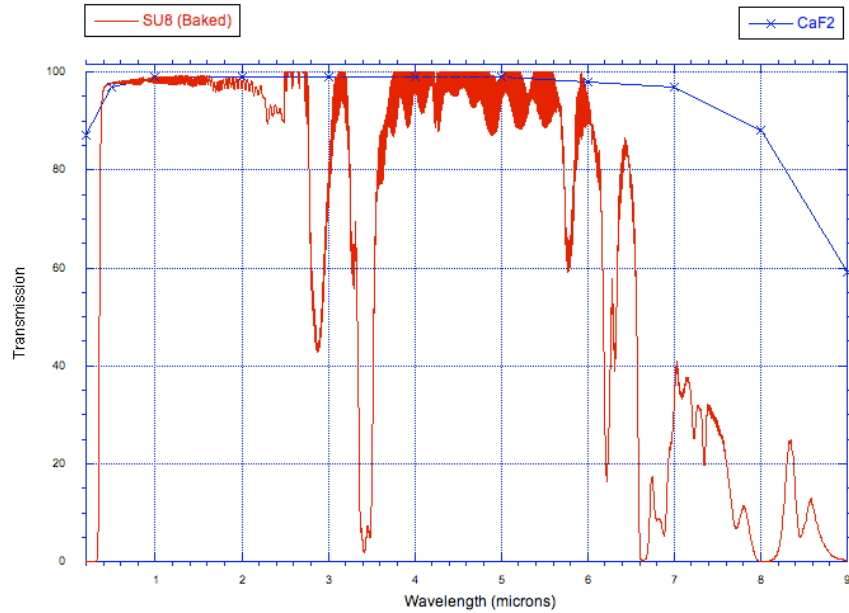


**Figure 3.1.** CaF<sub>2</sub> and SU-8 Transmission Spectrum in the Visible and Mid-Infrared Wavelength

Based on the availability of deposition techniques at PNNL, thermal evaporation, sputtering, and e-beam deposition methods were chosen as possible candidates for depositing CaF<sub>2</sub> onto silicon. CaF<sub>2</sub> films, with thicknesses ranging from 0.5 μm to 10 μm, were deposited using each method. Bi-layer 8.3-μm chalcogenide glass films were then deposited on the top of each of these CaF<sub>2</sub>-layered substrates. A tape-pull test technique (using 3M clear Scotch™ tape), derived from the ISO Standard 9211-4, was employed to examine film adhesion. Here, a tape of approximately 1 × 1 cm<sup>2</sup> was firmly pressed onto the coated films with sufficient tape remaining to execute a tape-pull test. Holding the sample in one hand and pulling the tape normal to the surface provides an assessment of the adhesion. Satisfactory adhesion was ascertained if the films survived at least ten tape-pulls without adhesion failure. Chalcogenide films on the CaF<sub>2</sub>-coated substrates resulted in satisfactory adhesion, while tape tests performed on bi-layers deposited directly on silicon failed after a few tape-pulls.

Coating a high-thermal expansion material on silicon substrates is a promising approach to improve chalcogenide film adhesion while preserving cleavability and high surface qualities of the silicon substrates. The drawback of vapor deposited CaF<sub>2</sub> films is that the films display a high degree of porosity, therefore, absorb water vapor easily and release it during post-deposition film annealing. An effective baking process is necessary to dehydrate CaF<sub>2</sub> films before glass deposition.

In a parallel effort, we employed a technique to improve film adhesion on silicon substrate by baking substrates at elevated temperatures for a prolonged period of time in a vacuum oven prior to chalcogenide glass deposition. The tape test resulted in an average of five pulls before the 4.5-μm-thick single As<sub>2</sub>S<sub>3</sub> layer failed. After we baked the substrates at 170°C for 3 to 12 hours in an inert environment, the tape test result on as-deposited 8.3-μm-thick bi-layer films improved to ten pulls without failing. Annealed films, however, still failed after the first tape pull. O’Hanlon (2003) indicates monolayer water’s residence time on metal is 10<sup>-5</sup> seconds at 450°C, 16 seconds at 100°C, and 9800 seconds at 22°C. The residence time is defined as the time a molecule spends on a surface before desorption. Because the

prebaked substrates are exposed to water vapor during loading into the vacuum deposition chamber, there is a need for a final in-situ baking within the deposition chamber.

Significant adhesion issues remain for annealed chalcogenide films. Cracks were often observed in annealed chalcogenide films. SEM/EDS measurements indicated no change in film stoichiometry after annealing; therefore, adhesion failure is not due to film compositional changes in cracks. It is likely that cracks and film failure is caused by excessive tensile stress produced by the thermal expansion of the films. To compensate for the tensile stress, a layer of polymer was coated on the chalcogenide films prior to annealing. Another layer of polymer can be used to overcoat the chalcogenide films to serve as a protection layer. Polymers usually contract during the curing process that restrains the tensile stress in the annealed chalcogenide films. The overcoat polymer layer also protects chalcogenide films from handling and moisture in the environment that is known to be responsible for chalcogenide film crystallization and degradation. We experimented with SU-8 photosensitive epoxies (MicroChem Corp.), which are routinely used as photoresist for micromachining and microelectronics applications. The SU-8 serial epoxies can achieve thicknesses from 0.5 to 200  $\mu\text{m}$  with a single coat. We found that the chalcogenide film with the SU-8 coating did not display cracks after annealing. The chalcogenide films adhered very well to the SU-8 coating and the cleaved facet quality was significantly better with improved overall film mechanical properties.

Because the polymer overcoat also serves as the film cladding, its transmission spectrum becomes important to the optical performance of the devices made in the chalcogenide films. We measured the transmission of cured SU-8, shown in Figure 3.1, from the visible to the mid-infrared wavelength using a Fourier transform infrared (FTIR) spectrometer. A transmission window of SU-8 between 4 and 6  $\mu\text{m}$  enables mid-infrared applications for this approach. Fluorinated polymers are available without the hydrocarbon stretch absorption peaks near 3.3  $\mu\text{m}$  and potentially others that have transmission extending further into the infrared. These results demand further exploration of these materials to enable additional design flexibility and improved mid-infrared device performance.

SEM/EDS characterization is used periodically to monitor the stoichiometry of the deposited chalcogenide glass films. It was previously confirmed that thermal evaporated chalcogenide glass films can maintain stoichiometry within 2% of the bulk parent material. To study the film adhesion and delamination characteristics, we used SEM/EDS to measure potential chemical diffusion between the deposited film layers and the substrate. The EDS data were analyzed using dot maps and line scans to provide atomic percentages across each film interface. For each interface, a 0.5- $\mu\text{m}$ -wide by 29- $\mu\text{m}$ -long area was extracted from each dot map for analysis. The extraction region is shown in Figure 3.2a for a 4.5- $\mu\text{m}$   $\text{As}_2\text{S}_3$  film on a Si substrate with a 1- $\mu\text{m}$ -thick  $\text{CaF}_2$  layer. The atomic percentage of each element on this film was calculated, corrected with the standard element correction, and then plotted in Figure 3.2b. The analysis shows significant diffusion of both arsenic and sulfur atoms into the  $\text{CaF}_2$  film layer, producing a molecular network with every two calcium atoms bonded to one arsenic and sulfur atom. In addition, greater numbers of Si atoms migrated across the  $\text{CaF}_2$  layer and diffused into the  $\text{As}_2\text{S}_3$  film. The atomic ratio of Si near the  $\text{As}_2\text{S}_3$ - $\text{CaF}_2$  interface was an unexpected 25%.

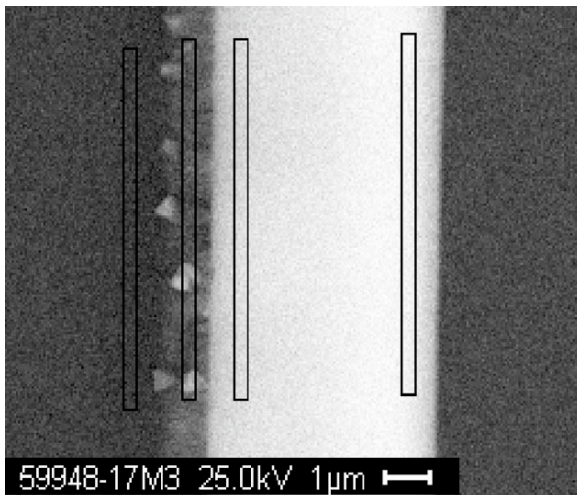


**Figure 3.2a.** Sections Across a Film and Substrate Interface were Chosen to Extract Atomic Percentage Data

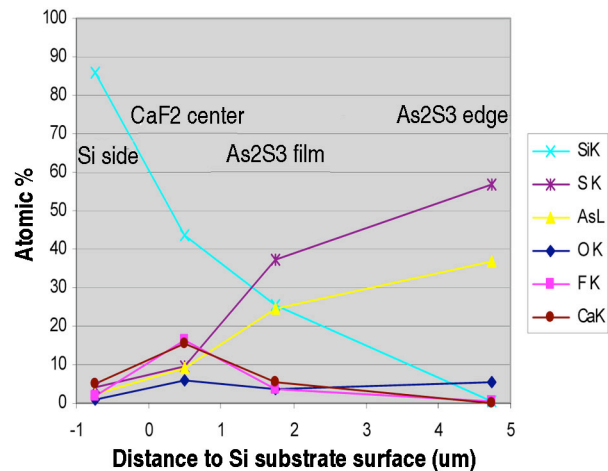


**Figure 3.2b.** Atomic Percentage of Elements in a Sample with a 1-µm-thick  $\text{CaF}_2$  Layer

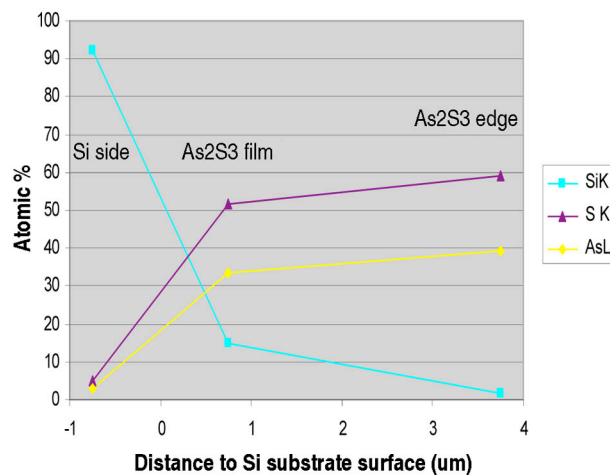


**Figure 3.2c.** Atomic Percentage of Elements in a Sample on a Si Substrate

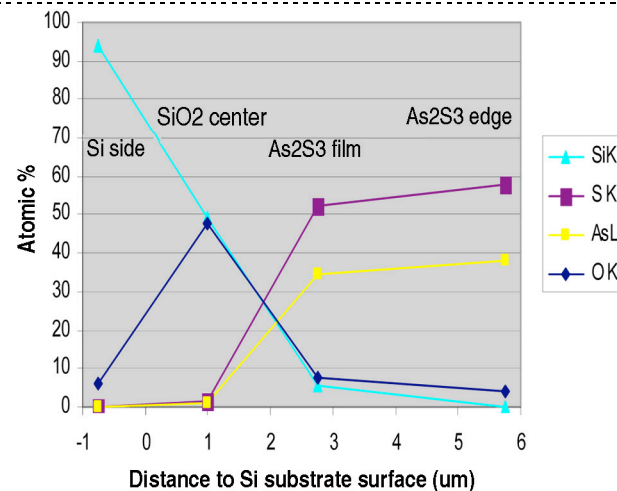


**Figure 3.2d.** Atomic Percentage of Elements in a Sample with a 2-µm-thick  $\text{SiO}_2$  Layer

This analysis was repeated on samples with  $\text{As}_2\text{S}_3$  films deposited on non-oxidized and oxidized ( $2\ \mu\text{m}\ \text{SiO}_2$ ) Si substrates. Atomic percentages of each sample are shown in Figure 3.2c and Figure 3.2d. The non-oxidized Si substrate exhibited smaller diffusion of 15% atomic ratio near the interface, compared to the previous  $\text{CaF}_2$  study. However, the chemical diffusion is significantly smaller for the oxidized Si substrate, where the atomic ratio of Si near the  $\text{As}_2\text{S}_3$ - $\text{SiO}_2$  interface is less than 5%. Arsenic or sulfur atom diffusion in the  $\text{SiO}_2$  layer was not detected. These results show that there is a correlation between the chemical diffusion magnitude at the film and substrate interface and the film adhesion behavior.

In a similar measurement of bi-layer chalcogenide films with a SU-8 overcoat, we detected arsenic and selenium atoms in the SU-8 near the  $\text{As}_2\text{Se}_3$  interface and a 20% carbon atomic ratio at the center of the  $\text{As}_2\text{Se}_3$  layer. The large chemical diffusion between these layers was again found to enhance the film adhesion. In contrast, low chemical diffusion, as seen in the oxidized Si substrate, results in poor film adhesion. Further analysis will be needed to study the degree of the chemical diffusion enhancement on film adhesion and potentially other chalcogenide glass film characteristics.

### 3.3 Film Characterization

In this section, film annealing characteristics were measured using both XRD spectrum shift and index of refraction change. Annealing chalcogenide films is critical to obtaining the desired optical performance in conjunction with material stability. The annealing process relaxes the crystalline structure to its lowest energy states. For as-deposit  $\text{As}_2\text{S}_3$ , annealing transforms  $\text{As}_4\text{S}_4$  crystal defects into  $\text{As}_2\text{S}_3$ .  $\text{As}_4\text{S}_4$  crystals are undesirable because their presence lead to high loss and instability of devices fabricated in these films. In this experiment, we annealed  $\text{As}_2\text{S}_3$  film at three different temperatures for three different durations at each temperature. The XRD spectrums of unannealed and annealed films are shown in Figure 3.3. The first peak of the unannealed film at  $15.4^\circ$  is aligned the realgar line ( $\text{As}_4\text{S}_4$ ), while annealing gradually shifts the peak toward  $18.5^\circ$ , the orpiment line ( $\text{As}_2\text{S}_3$ ). The hump peaking at  $29^\circ$  in the unannealed sample moves out to  $33^\circ$ , another orpiment line, and broadens with annealing. The shift of the film spectrum peaks towards those of the  $\text{As}_2\text{S}_3$  bulk glass with increasing temperature and duration enables the optimization of the annealing parameters.

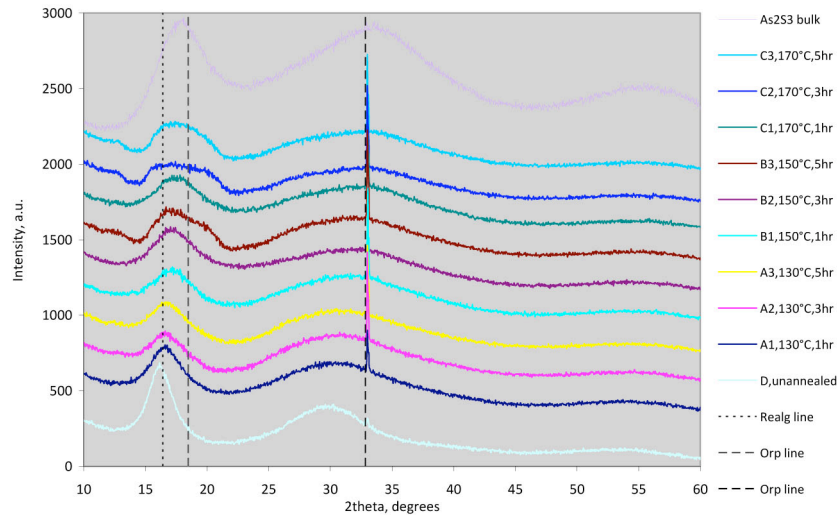


**Figure 3.3.** XRD Spectrum of Unannealed and Annealed  $\text{As}_2\text{S}_3$  Film Using Different Annealing Parameters

Photomodification is a process commonly used to alter the refractive index of chalcogenide films but the films must be fully annealed to produce stable results. Unannealed chalcogenide glass film has a lower refractive index than its bulk material, while annealing increases the refractive indices of chalcogenide glass films. We measured the refractive indices of unannealed and annealed films using a

1.55- $\mu\text{m}$  laser and the custom-built Metricon prism coupler having  $5 \times 10^{-4}$  resolution. Figure 3.4 shows that the refractive indices of  $\text{As}_2\text{S}_3$  films approach the bulk value with progressive annealing. Clearly the measurement of the refractive index provides an excellent monitoring tool to guide the film annealing process.

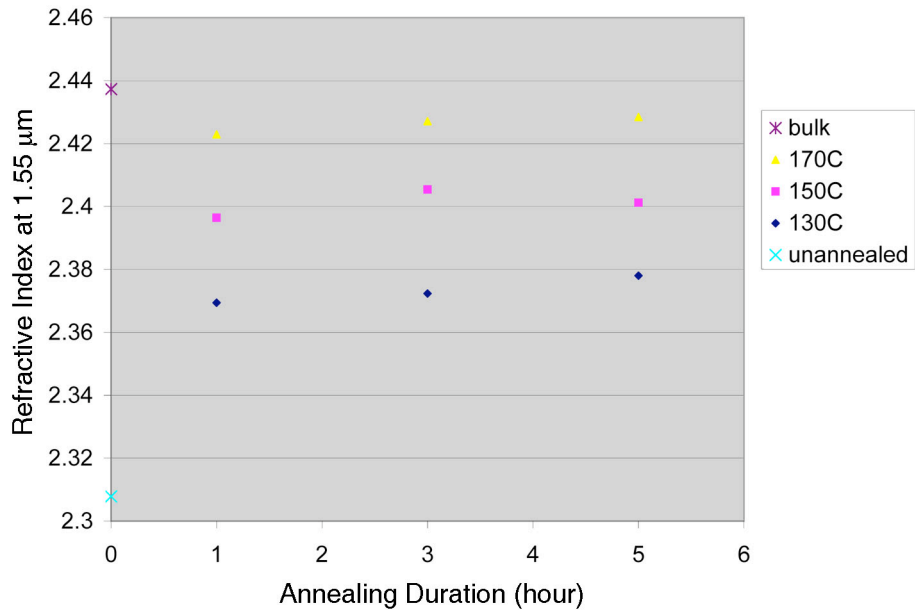


**Figure 3.4.** Refractive Indices of Unannealed, Annealed  $\text{As}_2\text{S}_3$  Films and Bulk Material

## 4.0 Lens Design for QC Laser High Heat Load Package and Waveguide Coupling

### 4.1 Preliminary Considerations

Earlier QC laser characterization work (Bernacki et al. 2008b) established the design criteria for collimation of QC lasers. Due to their waveguide design, QC lasers exhibit large divergence in the direction normal to the waveguide structure (fast axis) and a correspondingly smaller divergence in emission direction parallel to the waveguide structure (slow axis) (Krishnaswami et al. 2008b). Typical values for Full Width at Half Maximum (FWHM) divergence are  $62^\circ \pm 2^\circ$  and  $32^\circ \pm 2^\circ$  for the fast and slow axes, respectively. These values correspond to  $1/e^2$  divergence half angles of  $52.7^\circ$  and  $27.2^\circ$ , respectively. It is helpful to translate the FWHM values to  $1/e^2$  numbers because estimates of beam performance, like divergence and beam size, all depend on measurements with respect to  $1/e^2$  parameters.

The  $52.7^\circ$  divergence angle in the fast axis is the pacing factor for determining how large the numerical aperture must be to capture the laser emission efficiently. This divergence angle corresponds to a  $1/e^2$  numerical aperture of 0.8, but we set the numerical aperture at 0.85 to ensure some engineering margin for the design. Numerical aperture (NA) is defined as the sine of the angle formed by the edge or marginal ray emitting from the laser facet. Our design value equals the NA of high performance microscope objectives. Mechanical constraints limit the outer diameter (OD) of the lens to 5 mm in order to fit within the confines of the high heat load (HHL) package. Additionally, we must ensure that there will be sufficient working distance to mount the lens and manipulate it in the vicinity of the laser facet. We chose germanium as the lens material due to its high index of refraction and ease of single point diamond turning, which is essential to obtaining reasonably priced aspheric lenses in relatively small quantities needed for research tasks. Design of the lens and its performance, both modeled and measured, follows.

### 4.2 0.85 Collimating Lens

The resulting design of the 5-mm OD 0.85 NA collimating lens is shown below in Figure 4.1. The design utilizes a 10<sup>th</sup> order aspheric shape on the first (left) surface, and requires only a spherical concave shape on its second surface (closest to the laser). The mathematical expression used to describe the aspheric surface is shown in the following expression, where  $r$  is the radial coordinate,  $k$  is the conic constant, and  $R$  is the base radius of curvature of the surface.

$$z(r) = \frac{\frac{r^2}{R}}{1 + \left(1 - \sqrt{(1+k)\frac{r^2}{R^2}}\right)} + a_2 r^2 + a_4 r^4 + a_6 r^6 + a_8 r^8 + a_{10} r^{10}; r = \sqrt{x^2 + y^2}$$

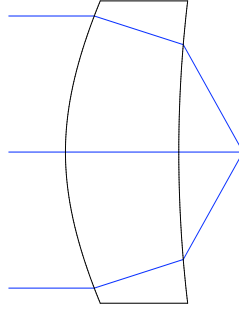


**Figure 4.1.** Layout Drawing Showing the Final Design for the Meniscus-Shaped Germanium (Ge) Collimating Lens

The design is summarized in Table 4.1.

**Table 4.1.** Design Summary for the 0.85 NA Germanium Collimating Lens

Parameter	Value
Material	Germanium
RMS WFE	$< 0.006 \lambda$ on-axis
Design Wavelength	8.5 $\mu\text{m}$
Central Thickness	2.0 mm $\pm$ 0.025 mm
OD	5.0 mm $\pm$ 0.050 mm
Effective Focal Length (EFL)	1.72 mm
Working Distance	1.135 mm
Numerical Aperture	0.85
Surface 1 Radius of Curvature (ROC)	4.413145 mm (convex)
Surface 1 Aspheric Coefficients	$a_4 = -4.682680\text{E-}003$ $a_6 = +1.056326\text{E-}004$ $a_8 = -2.319990\text{E-}006$ $a_{10} = -1.083806\text{E-}007$
Surface 2 ROC	20 mm (concave)

The design was optimized for both on-axis and off-axis rays up to 10  $\mu\text{m}$  off-axis. Practically, this means that the laser facet can be misaligned from the nominal optical axis of the lens by up to  $\pm 10 \mu\text{m}$  and still be diffraction-limited. This can be shown by looking at a metric of the performance of a lens with respect to the root mean square (RMS) wavefront error (WFE), the Strehl Ratio. Briefly, the Strehl Ratio is the ratio of the point spread function on-axis intensity of a system compared with the ideal value of the on-axis point spread function. A perfect system has a Strehl Ratio of one. The system is said to be diffraction limited if its Strehl Ratio is greater than 0.8, which equates to an RMS WFE of  $\lambda/14$ . The plot below shows that the system still gives acceptable performance for a translation of the lens from its true optical axis by a bit more than  $\pm 10 \mu\text{m}$ . The point of all this is to plan for the inevitable imperfections that arise in the fabrication of the opto-mechanical components needed to construct a practical system, as well as the limits on one's ability to place components in precise alignment. The plot in Figure 4.2 illustrates this point succinctly.

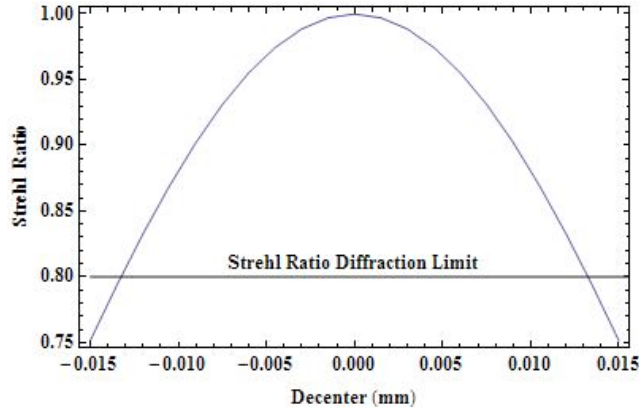


**Figure 4.2.** Plot of Strehl Ratio versus Lens Translation from its Optimum On-Axis Position. Notice that a translation of greater than  $\pm 10 \mu\text{m}$  can be tolerated before the lens system ceases to be diffraction limited. This engineering margin ensures that a reasonable opto-mechanical system will meet the requirements for diffraction limited performance.

### 4.3 0.85 NA Lens Testing Results

Although the 0.85 NA design is not new to FY08 work, additional lenses were procured to populate the predicted number of HHL packages required for other supported NA-22 projects. For the final lens order, 26 0.85 NA lenses having the 5-mm OD were manufactured using single-point diamond turning of germanium, and were also anti-reflection (AR) coated for  $R_{\text{ave}} < 1\%$  from 8 to 12  $\mu\text{m}$ . All lenses were tested in double-pass transmission at 9.4  $\mu\text{m}$  using a Twyman-Green interferometer described in previous reports. The 26 lenses had a mean RMS WFE of  $0.0165\lambda \pm 0.0037\lambda$ , which is much better than the diffraction-limited value of  $0.071\lambda$ . A plot of the RMS WFE values is shown in Figure 4.3. The lenses showed particularly good performance with regard to spherical aberration, and displayed an average Strehl Ratio of  $0.99 \pm 0.01$ , which greatly exceeds the diffraction limit threshold of 0.80.

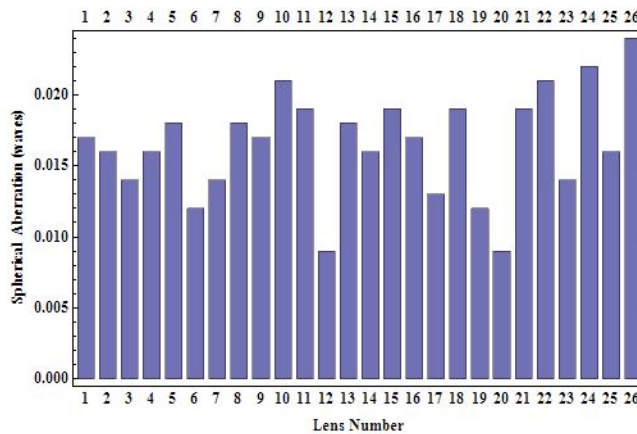


**Figure 4.3.** Bar Chart Showing the Measured RMS WFE Values for the Twenty-Six 0.85 NA Germanium Collimating Lenses Designed Expressly for the HHL Package Requirements. The mean RMS WFE was  $0.0165\lambda \pm 0.0037\lambda$ .

## 4.4 0.85 NA Collimating Lens Optimized at 5 $\mu\text{m}$

The collimating lens described thus far was optimized for use at 8.5  $\mu\text{m}$ , but certainly can provide diffraction-limited performance from approximately 6  $\mu\text{m}$  to 12  $\mu\text{m}$  in wavelength, but its performance degrades at wavelengths shorter than 6  $\mu\text{m}$ . Due to project requirements for the design of a chalcogenide waveguide beam combiner operating at approximately 5  $\mu\text{m}$  in wavelength, the 0.85 NA lens was re-optimized to provide diffraction-limited performance at 5  $\mu\text{m}$ . The design followed the same guidelines discussed in the section above on collimator lens design. The design for the optimized 5- $\mu\text{m}$  device is summarized in Table 4.2. The shorter wavelength design showed approximately equal sensitivity to element decenter as the 8.5- $\mu\text{m}$  HHL collimating lens design, maintaining diffraction-limited performance for element displacement up to  $\pm 9 \mu\text{m}$  from the nominal optical axis. A plot of this relationship is shown in Figure 4.4.

**Table 4.2.** Design Summary for the 0.85 NA HHL Collimating Lens that was Optimized for Use at a Wavelength of 5  $\mu\text{m}$

Parameter	Value
Material	Germanium
RMS WFE	$< 0.009 \lambda$ on-axis
Design Wavelength	5.0 $\mu\text{m}$
Central Thickness	2.0 mm $\pm$ 0.025 mm
OD	5.0 mm $\pm$ 0.050 mm
Effective Focal Length (EFL)	1.80 mm
Working Distance	1.133 mm
Numerical Aperture	0.85
Surface 1 Radius of Curvature (ROC)	4.047790 mm (convex)
Surface 1 Aspheric Coefficients	$a_4 = -3.382850\text{E-}003$ $a_6 = +3.635408\text{E-}006$ $a_8 = +2.032581\text{E-}007$ $a_{10} = -3.583678\text{E-}007$
Surface 2 ROC	10 mm (concave)

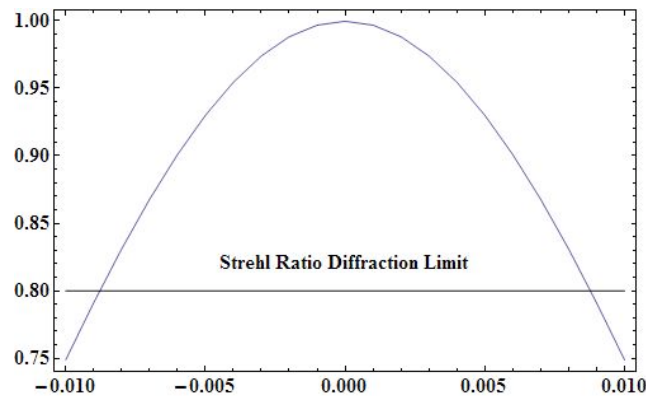


**Figure 4.4.** Change in RMS WFE as a Function of Element Decenter. Note that diffraction-limited performance obtains up to displacement values of  $\pm 9 \mu\text{m}$ .

## 4.5 0.85 NA Collimating Lens Optimized at 5 $\mu\text{m}$ Test Results

Eight lenses were manufactured using the design described previously by single-point diamond turning. The AR coating design provided  $R_{\text{ave}} < 5\%$  from 3 to 12  $\mu\text{m}$ . All lenses were tested in transmission at a wavelength of 9.4  $\mu\text{m}$  (the lowest wavelength accessible on the tunable  $\text{CO}_2$  laser used in the Twyman-Green interferometer), and exhibited diffraction-limited performance with an average RMS WFE of  $0.018\lambda \pm 0.005\lambda$ . The lenses also exhibited an average Strehl Ratio of  $0.99 \pm 0.01$ , greatly in excess of the 0.80 threshold value for diffraction-limited performance. A graph showing the measured Strehl Ratio for each lens is shown in Figure 4.5.

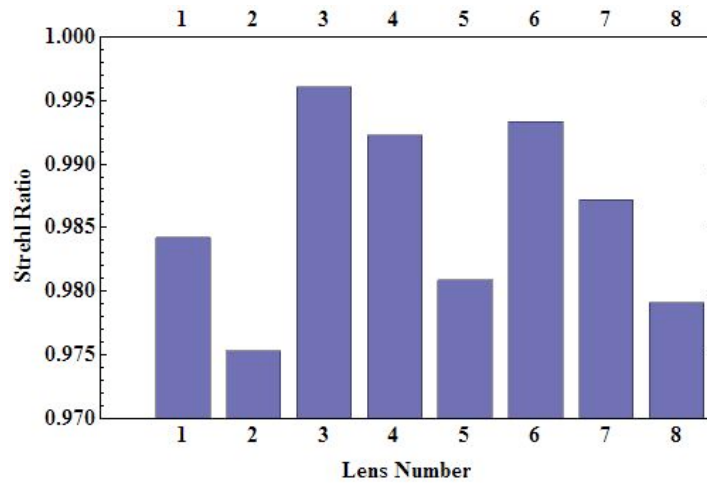


**Figure 4.5.** Value of Strehl Ratio for Each Lens Tested for the HHL Collimating Lens Optimized for Use at 5  $\mu\text{m}$ . Note that all of the lenses' performance far exceeds the diffraction-limit threshold of 0.80.

## 4.6 0.6 NA Fiber/Waveguide Coupling Lens

For practical applications of a collimated QC laser output, the light typically must be focused to probe or couple the light into a waveguide or optical fiber. Coupling into optical fibers or waveguides differs slightly on whether the device is single mode or multimode. Multimode fiber coupling requires that two criteria be met simultaneously:

1. The size of the focused spot must be smaller than the active core of the waveguide or fiber.
2. The numerical aperture of the focused beam must be less than the numerical aperture of the waveguide or fiber.

A diffraction-limited optical system ensures that we focus the light to a small enough spot, but due to the limits of physical optics, the minimum spot size that we can achieve is limited by the wavelength of light and the numerical aperture of the lens in use. Spot size is approximately given by the expression below.

$$\text{spot size}_{\text{FWHM}} = 0.6 \frac{\lambda}{NA}$$

So, in the ideal case, a 0.6-NA lens used at 8.5  $\mu\text{m}$  can yield a theoretical spot size of 8.5- $\mu\text{m}$  FWHM, or about 14.5  $\mu\text{m}$  out to the  $1/e^2$  intensity value, for a beam diameter of 29  $\mu\text{m}$  at the  $1/e^2$  intensity points.

To couple into single-mode waveguides and fibers also requires meeting two criteria:

1. The focused spot must be smaller than the core of the single-mode device.
2. The focused beam must be mode matched to the waveguide. This is practically accomplished by focusing using the same numerical aperture as the waveguide and ensuring that the focused spot be as aberration-free as practicable. Therefore, diffraction-limited performance and hence aspheric lens designs are paramount.

To handle the large range of currently available commercial chalcogenide fibers and waveguides under study, a lens numerical aperture of 0.6 was selected, along with maintaining an element OD of 5.0 mm to match that of the collimating lens. This design was also presented in the previous year's annual report, but is repeated here for completeness in describing the HHL optical system. The final design is summarized in Table 4.3.

**Table 4.3.** Design Summary for the 0.6 NA Fiber/Waveguide/Collimator Lens

Parameter	Value
Material	Germanium
RMS WFE	< 0.001 $\lambda$ on-axis
Design Wavelength	8.5 $\mu\text{m}$
Central Thickness	2.0 mm $\pm$ 0.025 mm
OD	5.0 mm $\pm$ 0.050 mm
Effective Focal Length (EFL)	3.07 mm
Working Distance	2.574 mm
Numerical Aperture	0.6
Surface 1 Radius of Curvature (ROC)	9.238746 mm (convex)
Surface 1 Aspheric Coefficients	a4 = -1.131846 -003 a6 = +1.972292E-005 a8 = -1.055187E-007
Surface 2 ROC	Infinite (plane)

The completed design is shown in Figure 4.6. The design was optimized to anticipate a lateral misalignment of  $\pm 25 \mu\text{m}$ , and shows diffraction-limited performance over a range nearly twice as large as this design goal. The increased tolerance is due to the reduced numerical aperture of the lens compared with that of the collimating lens. The variation in Strehl Ratio with lateral misalignment is shown in Figure 4.7. This design provides a generous engineering margin in the demands of placing and maintaining the lens in the optimum position for the intended application.

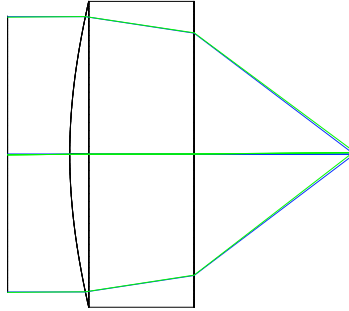


**Figure 4.6.** Optical Layout Showing the 0.6 NA Lens at Focus

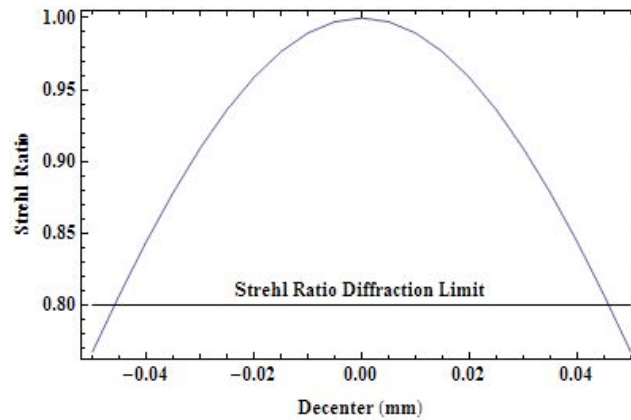


**Figure 4.7.** Plot of Strehl Ratio versus Element Decenter for the 0.6 NA Germanium Fiber Coupling Lens. Note that the lens can be decentered up to  $\pm 50 \mu\text{m}$  from its nominal optical axis and still display diffraction-limited performance.

The 0.85 NA HHL collimating lens and 0.6 NA fiber/waveguide coupling lens form a compatible lens pair that are optimized for use with the HHL package. Both exhibit performance in excess of the diffraction limit and show good tolerance to misalignment that occurs in the course of integration of opto-mechanical elements.



## 5.0 QC Laser Transmitter Integration

Early QC laser systems required cryogenic cooling in conjunction with large and complex opto-mechanical components. These limitations hindered their integration within field-deployable infrared sensing platforms. However, recent progress in QC laser design and fabrication has led to the introduction of room-temperature devices that has enabled new approaches for miniaturization and integration.

### 5.1 Design Goals, Approach, and Specifications

As a first step towards sensor miniaturization, PNNL's goal is to develop a fully ruggedized and compact QC laser transmitter by leveraging the optical and electronic component technologies developed for the telecommunications industry. Our approach utilizes the industry standard HHL laser component package, which is capable of providing the required laser thermal control. The hermetically sealed HHL package contains the QC laser die, a custom collimation lens, and the custom opto-mechanical mounting components. This design is compatible with QC laser dies mounted on both industry-standard C-mounts and custom submounts. The QC laser submount and the collimation lens are externally assembled onto a miniature optical bench (optical top plate) using small machine screws. This assembly approach facilitates QC laser collimation outside of the HHL package. Upon collimation, the miniature optical bench is mated to the cold plate within the HHL package using small machine screws. This method of assembly allows rapid turnover and rework, if necessary. A square thermoelectric cooler (TEC) module with an area of 256 mm<sup>2</sup> and heat pumping capacity of 28 W was selected to remove the excess heat produced by the QC laser. The cold plate is bonded to the TEC cold side using indium solder. An AR-coated ZnSe wedged window is used as an exit port for the collimated QC laser beam. Prior to sealing the HHL lid, the package is purged with ultra-pure argon gas to provide a dry and inert environment for operations up to a set point temperature of 0°C. A miniature ball valve (Beswick Engineering, model M3SV) is mounted under the electrical feedthrough pins to facilitate purging and venting the HHL package.

### 5.2 Packaging and Collimation Investigation

To test the performance of the HHL QC laser transmitter package, a 5.3- $\mu$ m distributed feedback (DFB) QC laser was obtained from Maxion Technologies, Inc. The C-mount QC laser was mounted in the HHL package along with the germanium asphere collimation lens described in Section 4.4. The assembled QC laser transmitter is shown in Figure 5.1. Laser collimation was performed using the hardware described in the prior year's final report. A lid was sealed to the HHL package, but a 5.3- $\mu$ m AR-coated window was not available in time for our device characterization. To minimize the effect of air currents, a 25-mm-long tube was temporarily fastened to the HHL output port.

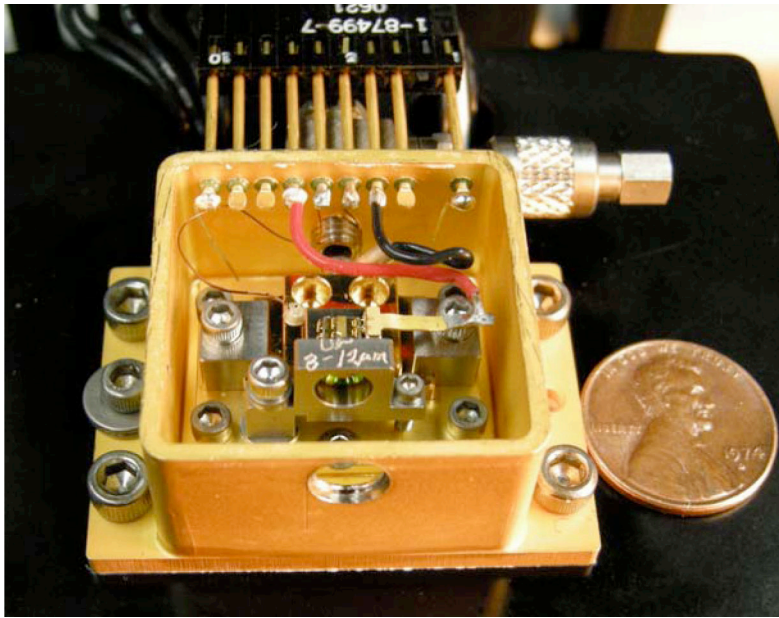


**Figure 5.1.** DFB QC Laser C-mount in a HHL Package. The germanium asphere collimation lens is shown in the flexure mount. A miniature ball valve is seen on the back of the package.

A mid-infrared wavemeter (Bristol Instruments, model 621) was used to characterize the emission wavelength as a function of both temperature and injection current. The optical power and room temperature was also monitored. Figure 5.2a shows the emission wavelength versus operating temperature. The QC laser was operated at 700 mA CW injection current while the setpoint temperature was adjusted in  $\pm 0.5^\circ\text{C}$  steps between 15 and  $20^\circ\text{C}$ . The emission wavelength was found to increase linearly with temperature by  $0.423 \text{ nm}/^\circ\text{C}$  and the power decreased by  $2.9 \text{ mW}/^\circ\text{C}$ . The drop in emission power near  $15^\circ\text{C}$  is due to a nearby water vapor absorption peak. Figure 5.2b shows the emission wavelength versus injection current. The QC laser was held at  $20^\circ\text{C}$  while the setpoint current was adjusted in  $\pm 2 \text{ mA}$  steps between 696 and 710 mA. The emission wavelength was found to increase linearly with injection current by  $0.035 \text{ nm}/\text{mA}$  and the power increased by  $0.407 \text{ mW}/\text{mA}$ .

The longitudinal mode profile was characterized using a FTIR spectrometer (Bruker, model Vector 22). FTIR spectra having  $0.5\text{-cm}^{-1}$  resolution was collected near threshold at 2 mA injection current increments. The QC laser was held at  $20^\circ\text{C}$ . The emission profile without the collimation lens installed, shown in Figure 5.3a, indicates multimode behavior. In contrast, the emission profile with the collimation lens, shown in Figure 5.3b, suggests single mode emission behavior. The AR-coated germanium collimation lens (BBAR 3 to  $12 \mu\text{m}$ ) had a 2% nominal reflection at  $5.3\text{-}\mu\text{m}$  wavelength. The recorded longitudinal mode profile suggests that the native DFB feedback is insufficient to provide stabilized single-mode emission. The 2% reflection from the collimation lens produced additional feedback and, within the FTIR measurement resolution, provided the desired single-mode structure. It was also noted that the DFB QC laser was quite sensitive to feedback from external optical elements, which provided further evidence that the DFB design produced weak feedback stability.

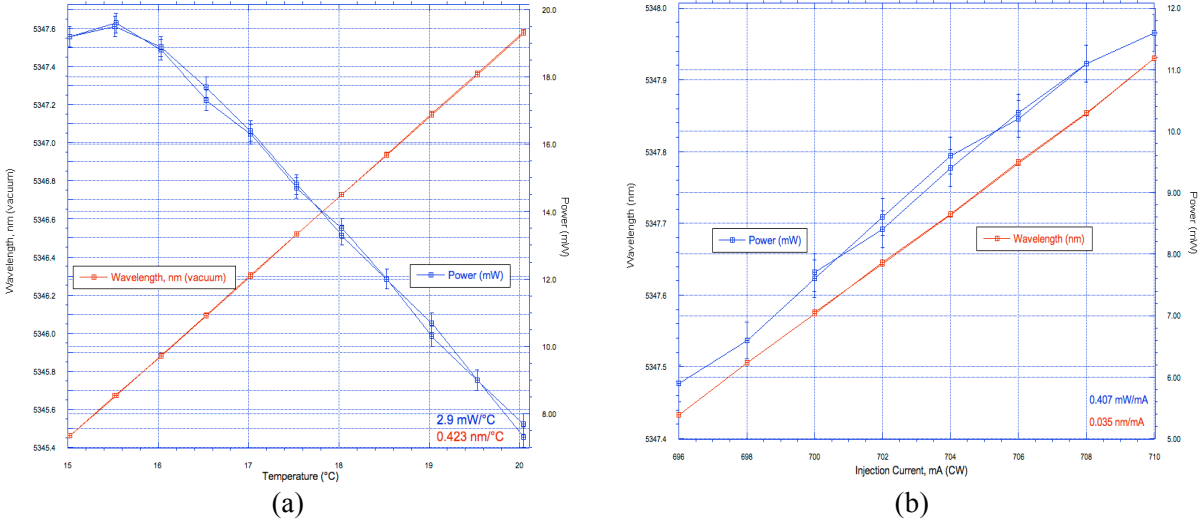


**Figure 5.2.** (a) Emission Wavelength versus Temperature at a Fixed Injection Current, and (b) Emission Wavelength versus Injection Current at a Fixed Temperature

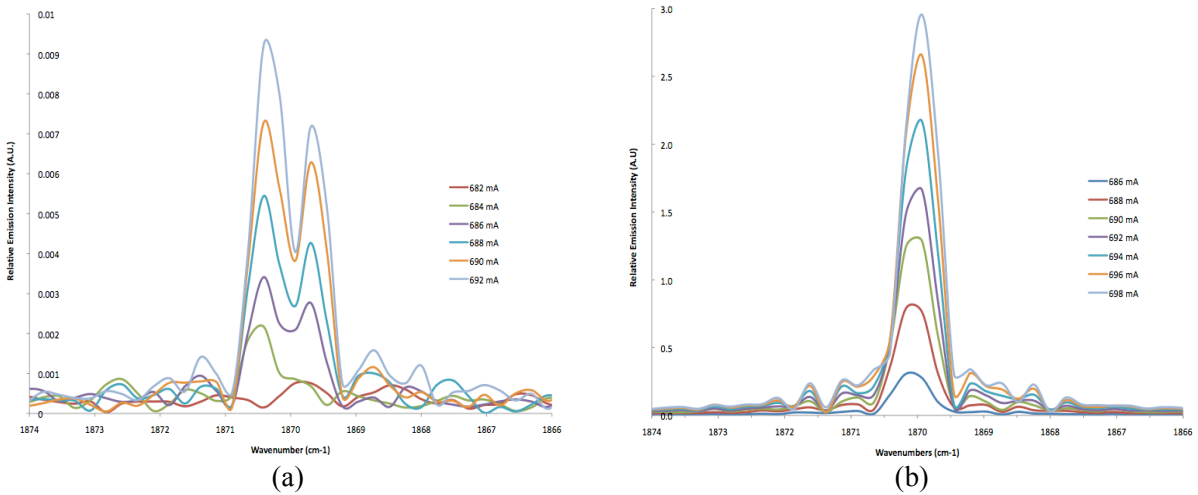


**Figure 5.3.** (a) FTIR Spectra Showing Multimode Behavior without Collimation Lens Installed, and (b) FTIR Spectra Suggesting Single-Mode Behavior with Collimation Lens Installed

We next characterized the long-term laser stability. The QC laser was operated at 20°C and 700 mA CW injection current, resulting in 7 mW output. Figure 5.4a shows the data trend over a 90-hour duration. The wavelength shifted upward by 3.6 ppm during this period. Expanding the data region between hours 10 and 11, as shown in Figure 5.4b, reveals that a nominal 1°C room-temperature oscillation produced a correlated 1.3 ppm (0.007 nm or 73 MHz) peak-to-peak wavelength oscillation. After repeated power cycling, we found that the laser would return to the desired emission wavelength within  $\pm 0.005$  nm.

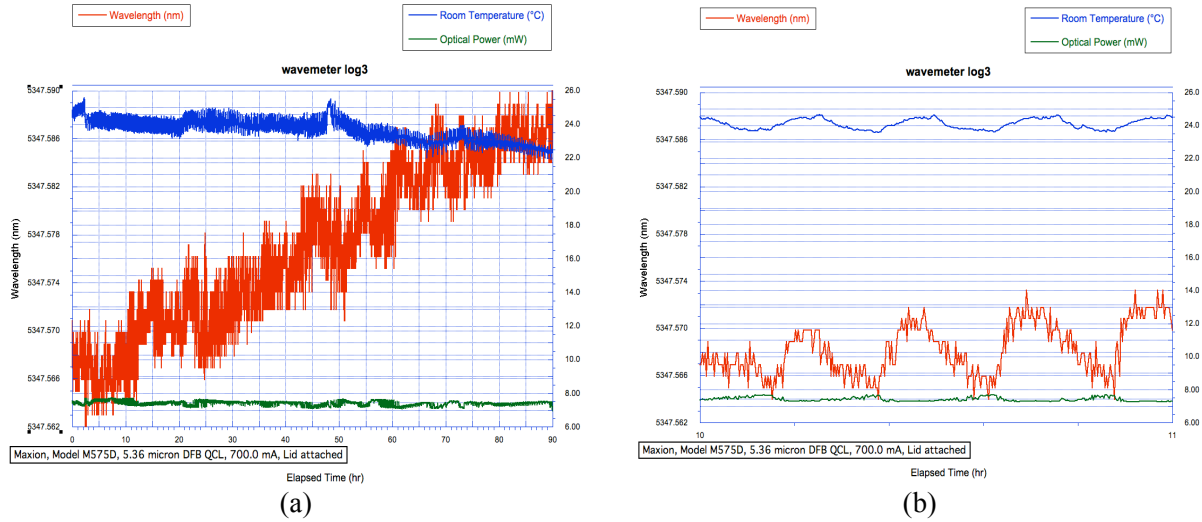


**Figure 5.4.** (a) Wavelength Drift over 90 Hours, and (b) A 1°C Room Temperature Variation Produced Nominally 1.3 ppm Peak-to-Peak Wavelength Shift

To evaluate the wavelength tuning performance of the HHL-packaged QC laser transmitter, spectra was collected from nearby water absorption features shown in Figure 5.5a. A nominal 1-meter path length was used at atmospheric pressure and the laser was operated just above threshold at 20°C. A  $\pm 50$  mA linear ramp swept the DFB QC laser wavelength through the strongest water absorption peak, producing the correlated loss in transmitted laser power as shown in Figure 5.5b.

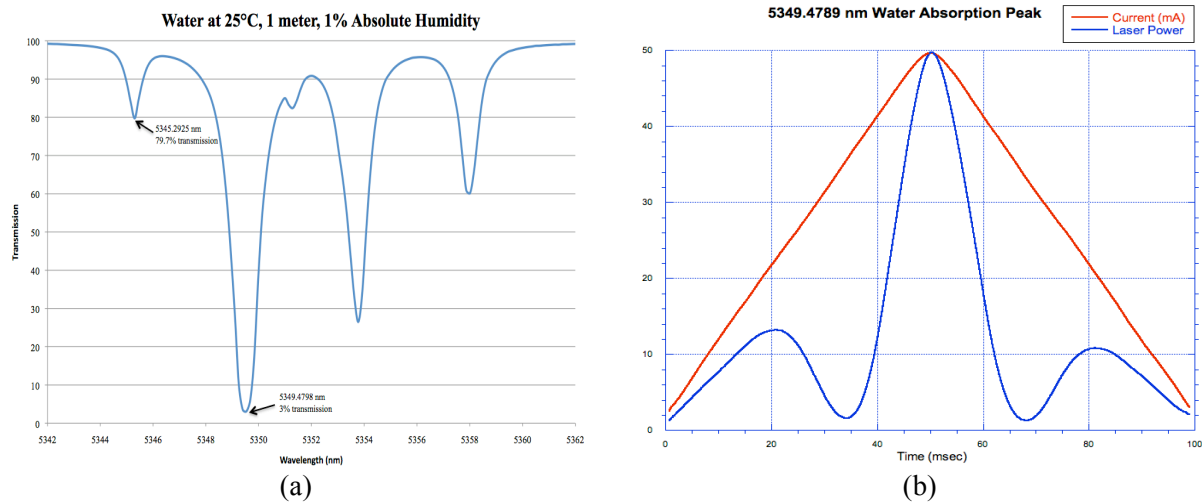


**Figure 5.5.** (a) HITRAN 2004 Water Spectrum (1 meter, 1% absolute humidity) within the DFB QC Laser Tuning Range; (b) Direct Transmission Trace of the Strong Water Line

### 5.3 HHL QC Laser Transmitter Design Update

Developing designs that incorporate QC laser devices requires careful attention to thermal design. The HHL package uses a large square TEC module with heat pumping capacity of 28 W to remove the excess heat produced by the QC laser. The selection of materials used for laser integration was based primarily on their thermal and mechanical properties. Oxygen-free, high-conductivity copper (OFHC) was selected for both custom and C-mount submount configurations. The remaining two components (optical top plate and cold plate) in the main thermal pathway require materials with optimum mechanical properties, such as hardness and stiffness, reasonable thermal conductivity, and materials with a CTE that is compatible with the TEC module. If the thermal expansion effects are not accounted for, the inevitable mechanical strains can quickly destroy the TEC module. The absolute value of the thermal expansion is proportional to the TEC module dimension, so the large (16 × 16 mm) TEC module used in our design requires materials with small differences in CTE. The TEC cold-side material is 100% Al<sub>2</sub>O<sub>3</sub> ceramic having 7.2 ppm/°C CTE. Our component materials ideally would have thermal conductivity near pure copper and a CTE near the TEC ceramics. Unfortunately, one must compromise on thermal conductivity to minimize the CTE mismatch. For example, copper has a thermal conductivity of 400 W/m/°K, but the CTE is an unacceptable 16.7 ppm/°C. Fortunately, specialty tungsten-copper alloys are available for this application (CMW Inc., Thermkon® 83). The alloy is composed of 75% tungsten and 25% copper. The thermal conductivity is a modest 190 W/m/°K, but has a CTE of 8.3 ppm/°C. The tungsten-copper cold plate is bonded to the TEC module cold side using indium solder with a melting point near 200°C. At room temperature, the mechanical strain on the TEC module is small because the expansion differential between the CTE and the cold plate is only 2.3 μm.

To maximize the thermal performance of the HHL package design, the mating surfaces of all the custom-machined HHL components were carefully finished to maximize flatness and minimize surface roughness. These components are important because they account for a majority of the thermal contact resistance between the QC laser heat source and the TEC. To achieve the desired thermal design performance, thermal mating surfaces are generally specified finished flat within ±25 μm across the entire mounting surface and smooth to a surface finish of 0.8 μm R<sub>a</sub> or better. R<sub>a</sub> is the arithmetic average of the roughness profile over a given distance. The as-machined and finished surfaces were characterized using a Veeco non-contact optical profilometer. Surface data was collected over a 150 × 115 μm<sup>2</sup> area and analyzed to provide both R<sub>a</sub> and R<sub>q</sub>. R<sub>q</sub> is the quadratic mean of the roughness profile and provides the most representative assessment of the magnitude of the varying roughness quantity.

The machined surfaces had a representative surface finish with 0.5 μm R<sub>a</sub> and 0.6 μm R<sub>q</sub>, but also had roughly ±1.0-μm periodic features produced by machining flycutter. All flat accessible surfaces were mechanically lapped with 0.025-μm diamond-oil slurry on a stainless steel cloth to remove the periodic features. This was followed by diamond-oil slurry on Pellon polishing cloth. The final polish was colloidal silica solution on cloth. This process removed all evidence of the periodic machining features and produced representative surface finishes having 0.4 μm R<sub>a</sub> and 0.5 μm R<sub>q</sub>.

The recessed submount surfaces that mated with the QC laser were not accessible to the lapping process described above. In addition, the machining process was incapable of producing zero radius corners at right-angle intersecting planar surfaces. To obtain intimate contact between the thermal surfaces of the QC laser mount and the submount, the residual radius at intersecting surfaces must be minimized. A 25.4-μm diameter wire electrical discharge machining (EDM) process was used to lap and

zero radius the recessed submount surfaces, as shown in Figure 5.6. By taking several machining passes, each with decreasing power,  $0.24 \mu\text{m} R_a$  and  $0.3 \mu\text{m} R_q$  microfinish was obtained. After surface finishing, all parts containing copper were Au plated by an external vendor to prevent oxidation.

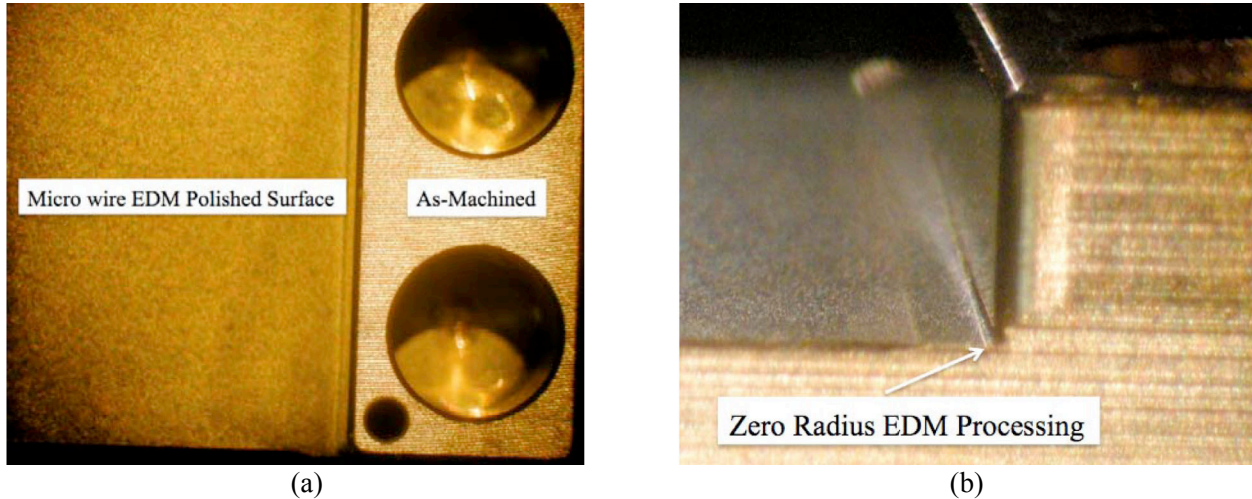


**Figure 5.6.** (a) Submount Component with Micro-Finished Surface; (b) Zero Radius Machined Mating Corner. Machining was performed using micro-wire EDM.

The HHL QC laser transmitter design described in the FY2007 report was updated so that it was compatible with pre-production QC laser assemblies delivered by Hamamatsu Photonics K.K., Laser Group (Japan). The laser die submounts are a design proprietary to Hamamatsu; therefore, we redesigned our OFHC submount assembly to accommodate the new laser. The exploded HHL assembly, with the new OFHC submount, clamp, and submount retainer design, is shown in Figure 5.7a. The fully assembled HHL transmitter is shown in Figure 5.7b. The submount retainer is polymer material fabricated using a rapid prototyping process. The retainer clamps the QC laser assembly tightly down to the OFHC submount, while simultaneously drawing it against the submount back ledge. This design provides secure mounting and thermal conduction from the bottom and back of the QC laser mount.

## 5.4 HHL Package Thermal Modeling

An important QC laser integration issue is thermal management because it affects both optical component stability and laser frequency stability. A thermal evaluation of the HHL QC laser package was performed using finite element simulation software (ANSYS Thermal Analysis System). The simulation software was used to analyze the thermal transfer aspects of a C-mount QC laser, the 1.5-mm-thick WCu optical top plate, a thermal grease layer, and the 1.5-mm-thick WCu cold plate bonded to the cold side of the TEC module. The thermal conductivities of Thermkon® 83, OFHC, and the thermal grease used were 190, 391.2, and  $2.5 \text{ W/m}^{\circ}\text{K}$  respectively. The model used a thermal grease thickness of 50 microns as recommended by prior research (Chia-Pin et al. 1997).

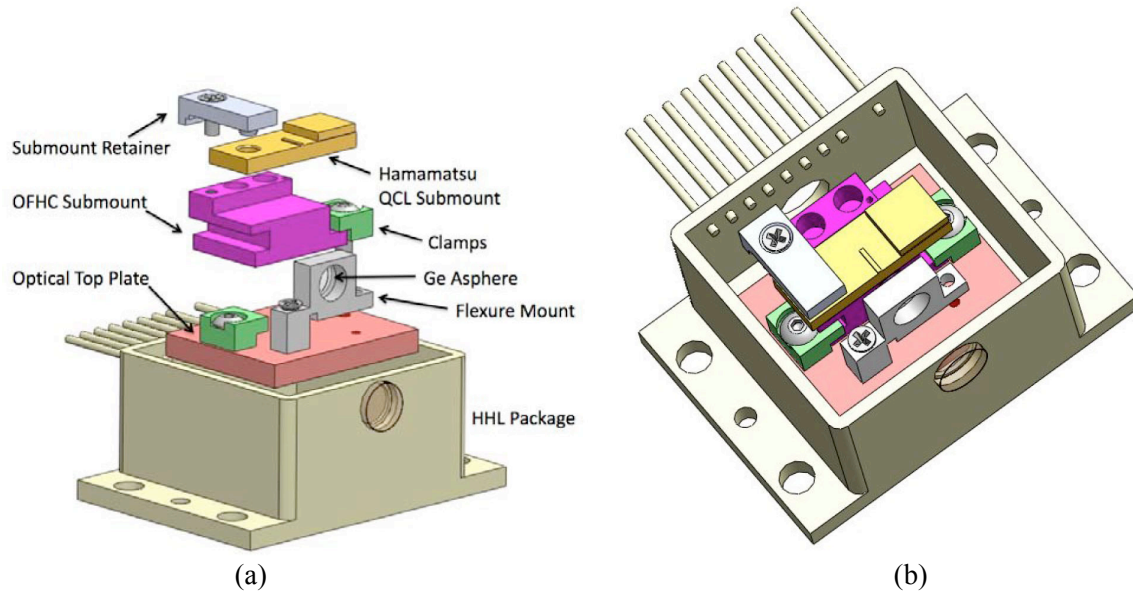


**Figure 5.7.** (a) Exploded and (b) Assembled HHL QC Laser Transmitter with Hamamatsu QC Laser Submount

The contact pressure between the C-mount and the submount must be as high and uniform as possible to provide good thermal conduction. The surface finish and flatness, as discussed in other sections of this report, are important parameters that affect the contact performance. A 2-56 machine screw retains the C-mount to the copper submount. The contact area between the C-mount and the submount is 6.35 mm by 5.21 mm, for a surface area of 33.1 mm<sup>2</sup>. Using an assembly torque of 22.6 Ncm will achieve 75% of yield for a stainless steel fastener with a yield strength of 2813 kg/cm. This will provide a clamping force of 153.5 Nm and a contact pressure of 15 MPa. Using this contact pressure and reported thermal experimental results (Rao et al. 2004) for copper-copper interfaces, the thermal contact conductance between the C-mount and the submount was estimated to be 200,000 W/m<sup>2</sup>/°K.

The QC laser was assumed to produce a 5-W heat load. The TEC cold side was held at a constant set point temperature so that the QC laser maintained a temperature of 10°C. The modeled assembly is shown in Figure 5.8a. The components include the WCu cold plate and optical top plate (shown in green) and the OFHC submount and laser C-mount (shown in orange). The QC laser die is represented in yellow. Figure 5.8b shows the critical thermal clamping surfaces.

Thermal simulations were iterated by varying the TEC cold-side temperature until the maximum temperature of the QCL was 10°C, using 0.5% error band on the heat balance. For this simulation, the split plate design thermal boundaries between the optical top plate and the cold-side plate were modeled using 50-μm-thick thermal conductive grease. The simulation results show that the TEC cold side must be maintained at 0.67°C to achieve a laser operating temperature of 10°C. The major thermal bottleneck is the native laser C-mount. A nominal 6.75°C gradient is shown in Figure 5.9 between the QC laser die and the C-mount back surface. The thermal gradient is only 2.75°C between the submount top and the TEC cold side. The location of the thermistor, used to provide temperature feedback to the TEC controller, is also shown in Figure 5.9. This simulation also showed that a large thermal gradient (~7°C) exists between the QC laser die and the thermal feedback location.

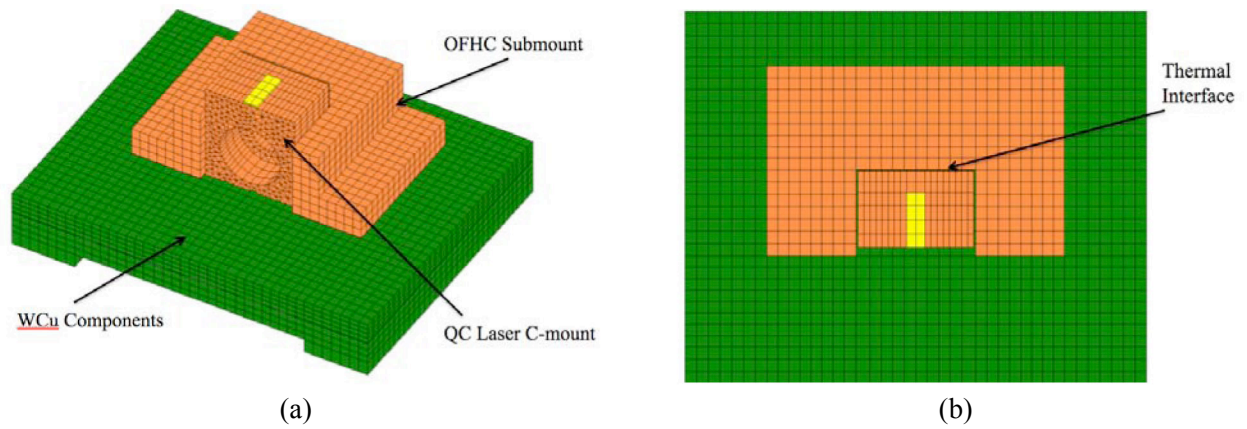


**Figure 5.8.** (a) Component Configuration Used in the Thermal Simulation; (b) Critical Thermal Contact Surfaces

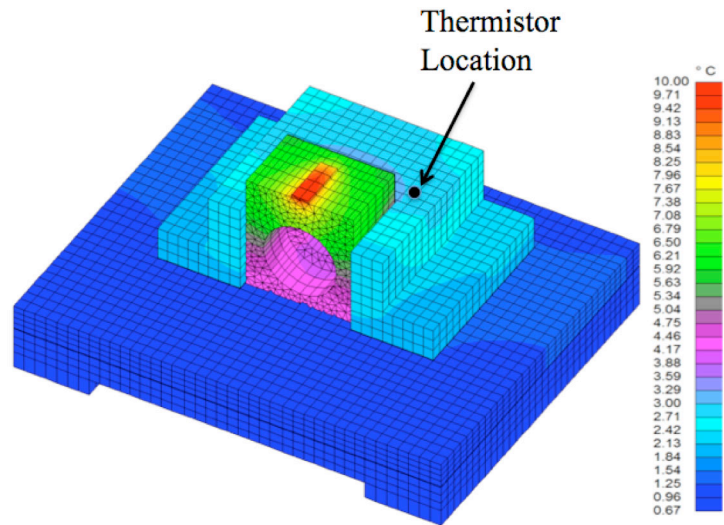


**Figure 5.9.** Temperature Distribution from Thermal Simulations

## 6.0 Chalcogenide Optical Fiber Research

Fiber optics components are highly desirable for integrated mid-infrared sensing systems. Yet the availability of commercial mid-infrared optical fibers is limited to several small companies producing small batches of highly specialized fiber. Because the market for mid-infrared fiber products is still in its infancy, there are no readily available tools or processes in place for fabricating mid-infrared fiber-optic components. Therefore, several tools commercially available for silica fiber processing were modified to process mid-infrared transparent chalcogenide optical fiber. To efficiently inject light into or couple light out of an optical fiber, the fiber facets require high quality optical surfaces. While processing tools are readily available to strip and cleave silica-based optical fibers, handling and processing chalcogenide glass fiber can be challenging because of its fragility. The following section describes the processing methods developed at PNNL to chemically remove the fiber jacket and to produce optical-quality facets by either cleaving or mechanical polishing.

### 6.1 Fiber Jacket Removal

The fiber used in this study was procured from CorActive (Quebec, Canada). This fiber (IRT-SE65) is fabricated from an arsenic selenide glass composition, having nominal core, clad, and jacket diameters of 70  $\mu\text{m}$ , 180  $\mu\text{m}$ , and 350  $\mu\text{m}$ , respectively. A protective jacket is formed during the fiber draw using thermally cured acrylate. To fabricate optical facets, the jacket must first be removed without damaging the fiber. Because of the fragile nature of the fiber, we developed a chemical-stripping method to expose the fiber instead of the mechanical jacket stripping techniques. The vendor recommended methylene chloride to dissolve acrylate jacket layer. However, our investigation showed that that methylene chloride had little reaction with the acrylate jacket under extremely long process times. We, therefore, proceeded to evaluate other chemical processes including concentrated acid and then commercial photoresist stripper.

In the first case, the fiber was first soaked in sulfuric acid having a concentration of 95.5%. Here, the jacket was unaffected by the acid bath until the temperature was elevated to 80°C. At this temperature, the jacket dissolved after 30–120 minutes soak time. Unfortunately, this fiber cannot handle high processing temperatures. The stripped fiber region had a tendency to curl after the long acid treatment.

Next, we used Nano-Strip™ solution, produced by Cyantek Corporation (Fremont, California), which is widely used to remove photoresist and organic contaminants in semiconductor industry. Our investigation showed that this Nano-Strip was very effective at removing the acrylate jacket within 1 to 2 minutes at a bath temperature of 80°C. In this case, the acrylate jacket quickly separated from the fiber so that it could be peeled away by set of tweezers. Because the fiber is maintained at an elevated temperature for a short duration, it does not get damaged. However, extending the soak time does produce fiber curl as observed in the case of sulfuric acid. After the jacket is removed, the stripped fiber is washed thoroughly in deionized water.

In addition to stripping the jacket from the fiber ends to facilitate the fabrication of the end facets, we were also successful in stripping away jacket sections in the middle of the fiber to provide access for additional fiber processing.

## 6.2 Fiber Cleaving Investigation

The end facets in the CorActive chalcogenide fiber were prepared using an ultrasonic FK11 cleaver available from Photon Kinetics (Beaverton, Oregon). Angle cleaves were prepared using a model FK12 angle cleaver ( $0^\circ$  to  $15^\circ$  range). Once again, these cleavers were designed for cleaving mechanically robust silica fiber rather than frangible chalcogenide optical fibers. Fortunately the design of the cleaver incorporates an adjustable precision tension mechanism that has the dynamic range to facilitate cleaving chalcogenide glass fibers.

The chalcogenide fibers are first stripped to expose a length of bare fiber such that a sufficient section can be held in place by the cleaver holding blocks. To produce acceptable cleaves with chalcogenide fibers, the fiber tension must be reduced from its factory 100 psi setting to approximately 60 psi, a metric that was arrived at empirically through a series of tests. If the tension is too high, the fiber tends to break once the diamond blade scores the fiber, producing a rough facet surface as shown in Figure 6.1(a). When the tension is less than 60 psi, the blade bends the fiber out without properly scoring it, producing the cleave depicted in Figure 6.1(b). To achieve the right tension while also preventing the fiber from bending outwards, a rigid flat metal bar was placed opposite of the scoring blade. This minor modification holds the fiber in place as the diamond blade moves through it scoring motion. This simple tool modification in conjunction with the appropriate tension reliably produces fiber cleaves like the one depicted in Figure 6.1(c).

Next, we focused our effort on producing angle cleaves using the FK12 angle cleaver. Due to differences in the cleaving tool, the parameters established for the straight cleaves were used only as a starting point for angle cleaving. A series of tests established that the appropriate tension setting for angled cleaves in chalcogenide fibers was 80 psi. Figure 6.2(a) shows the image of an angle cleave with small edge defects that do not propagate to the fiber core. Figure 6.2(b) provides a side view of the same fiber exhibiting a nominal  $8^\circ$  cleave angle. Increasing the tension beyond 80 psi begins to degrade the cleave properties.

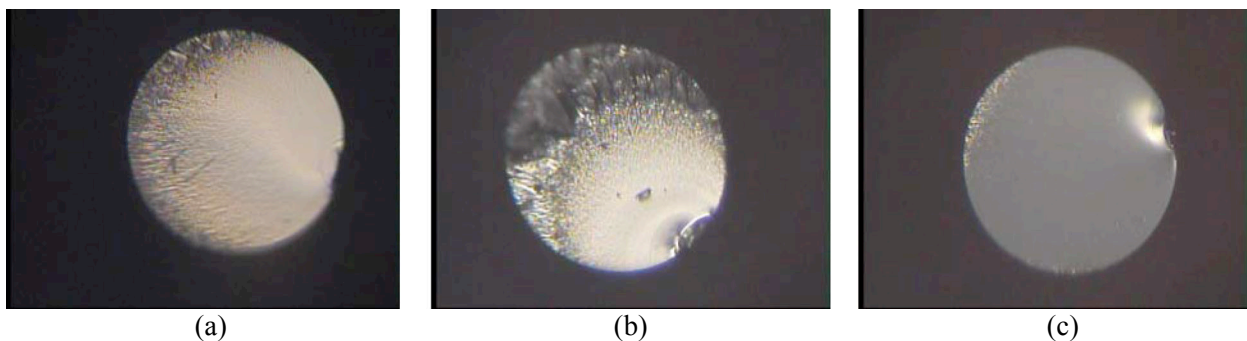


**Figure 6.1.** Images of the Cleaved Facet When Fiber Tension was (a)  $\sim 100$  psi, (b)  $< 60$  psi, and (c) 60 psi with Metal Bar Installed. It can be seen that both high- and low-fiber tensions leave rough and damaged cleave surfaces indicating the need to narrow in on the right fiber tension with the assistance of a metal bar.

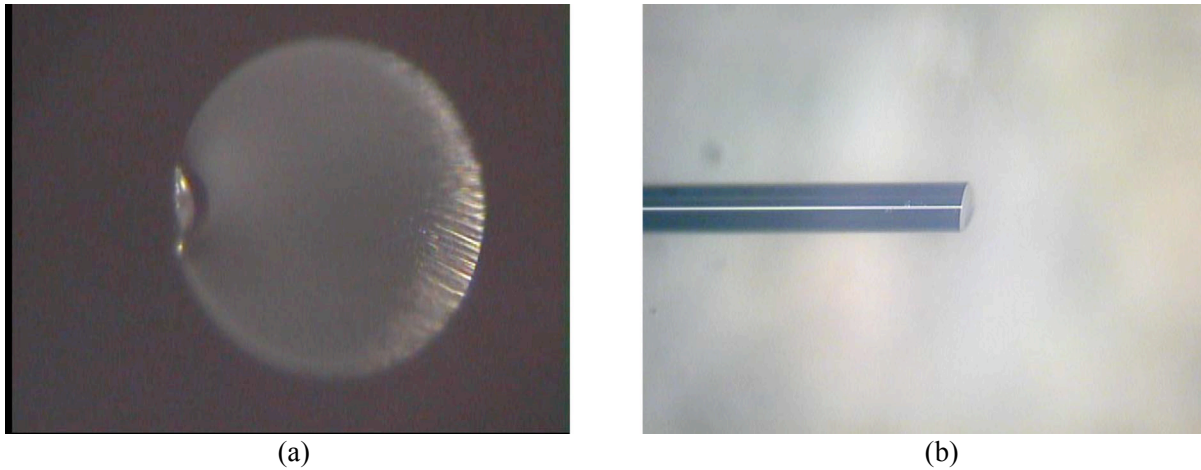


**Figure 6.2.** Images of Angle Cleaved Surfaces: (a) Top View and (b) Side View Obtained by Using Fiber Tension of 80 psi and the Metal Bar. Edge defects and scratches are outside the core region and do not impact the performance of the fiber.

### 6.3 Fiber Polishing Investigation

Another common optical fiber processing step is preparing fiber patch cords. The fiber is generally placed in a protective outer sheath and connectorized using telecom standard metal or ceramic fiber optic connectors. To assemble the connectors on the fiber patch cord ends, the stripped fiber end is epoxied into the connector and the end facets are created using an optical polishing process. Adapting chalcogenide fiber to patch cords fabrication follows the same steps as silica fiber, except extra care must be taken during the polishing process.

A Buehler FibrMet portable fiber optic polisher and aluminum oxide polishing pads with 12, 9, 3, 1, and 0.3  $\mu\text{m}$  grit sizes are used. The fiber is first ground with a 12- $\mu\text{m}$  polishing pad to remove the residual epoxy until the ferrule end is exposed as shown in Figure 6.3. The fiber facet is then polished to an optical finish using successively finer polishing pads. Chalcogenide glass is much softer than silica, so it can become easily scratched during the polishing process. Frequently spraying water onto polishing pads can significantly reduce fiber facet scratches. After each polishing set, the fiber facet is inspected under a microscope, and the resulting images are shown in Figure 6.3(a)–(e). When deep scratches larger than the polishing pad grit are observed, the polishing sequence must be restarted using the next larger polishing pad grit.

During the course of our process development, we found it critical to completely fill the connector ferrule with epoxy. If air pockets are formed between fiber and the ferrule interior wall, the fiber edges will fracture during polishing. The fractured chips then produce deep scratches on the polished surface. Both straight and angle polished fiber facets were successfully demonstrated using the described polishing method.

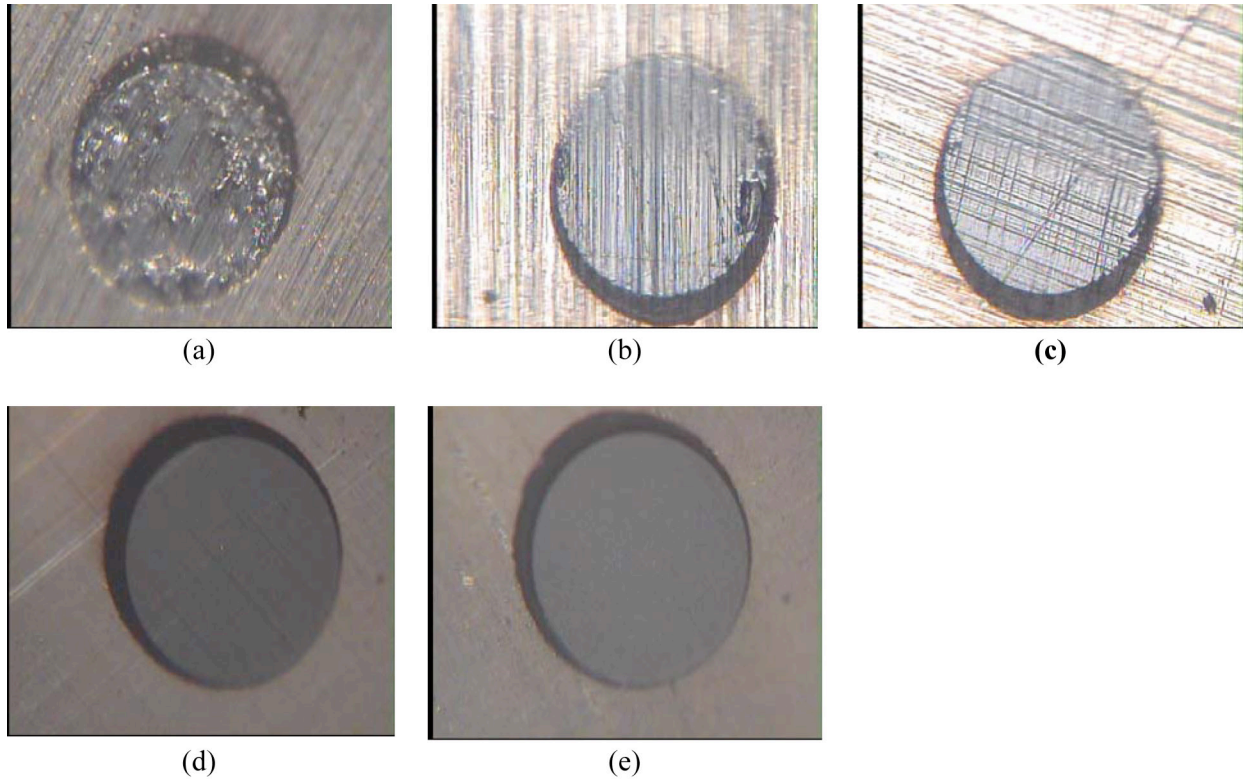
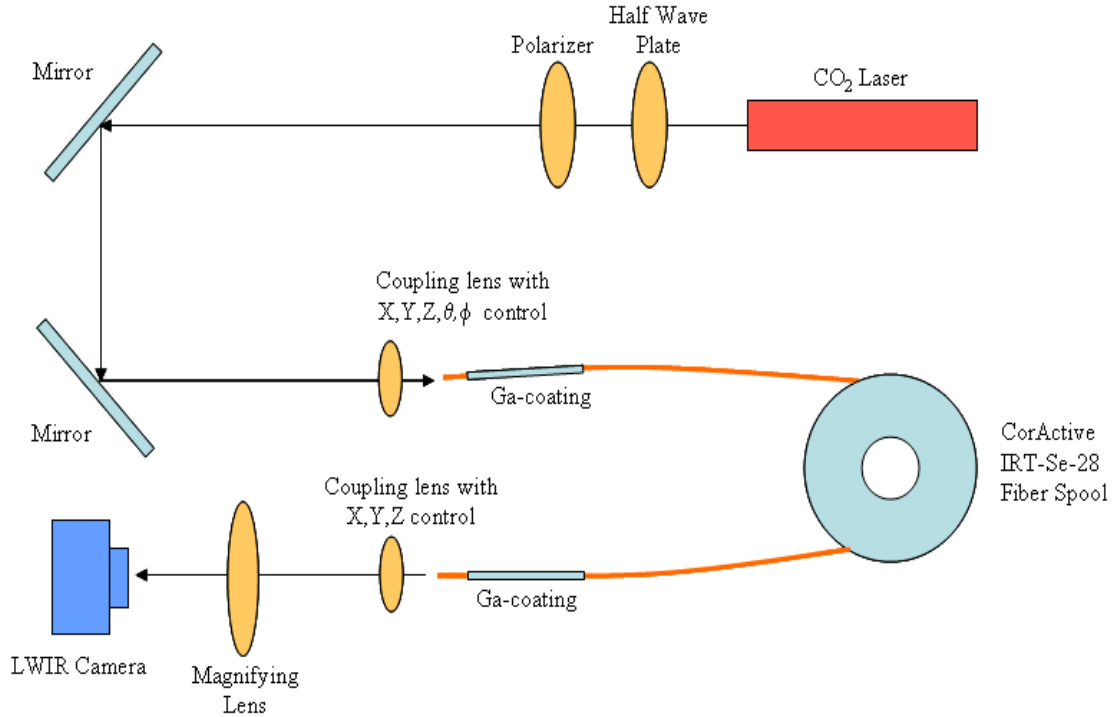


**Figure 6.3.** Fiber Facet after Polishing with (a) 12  $\mu\text{m}$ , (b) 9  $\mu\text{m}$ , (c) 3  $\mu\text{m}$ , (d) 1  $\mu\text{m}$ , and (e) 0.3  $\mu\text{m}$  Grits

## 6.4 Fiber Optical Characterization

Once we established a repeatable process for fabricating optical quality cleaves, we next characterized the performance of a single mode fiber optic cable (CorActive IRT-Se-28) having a core diameter of 28  $\mu\text{m}$ . Both ends of fiber were cleaved and inspected for facet quality and the acquired images were similar to those shown in Figure 6.1(c) above. The test apparatus comprised of a tunable  $\text{CO}_2$  laser, tuned to 9.3  $\mu\text{m}$  wavelength. A polarizer and half-wave plate were used in combination to function as an attenuator. The laser beam was reflected off a set of mirrors to provide flexibility in alignment as shown in Figure 6.4.

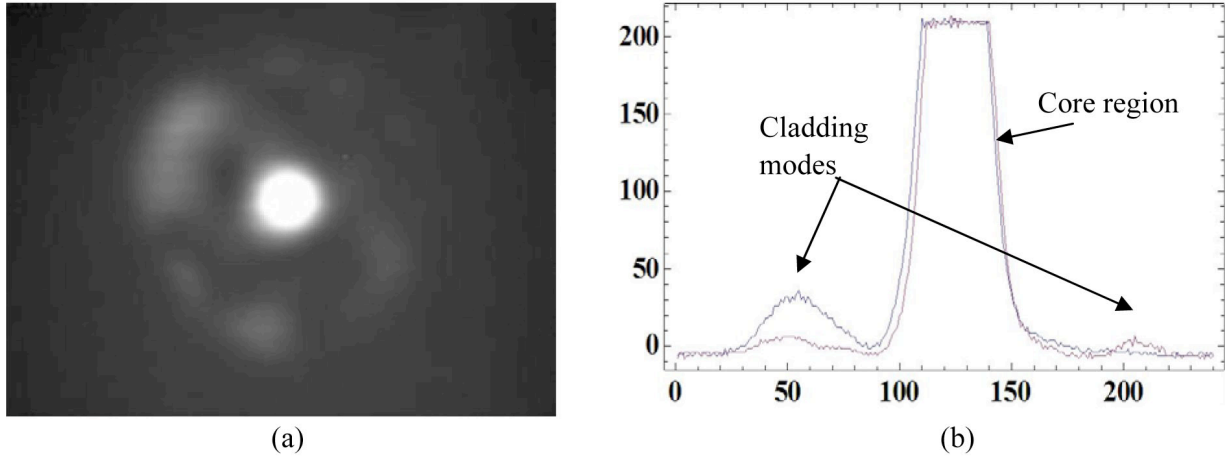
A 0.6 NA germanium aspheric lens with a focal length of 8mm was chosen as the coupling lens. This lens was mounted on a translation stage that provided five degrees of freedom. Similarly, the input facet of the fiber was also placed on a matching mount to provide complete flexibility and control of fiber orientation and to obtain the optimum coupling efficiency. The power at the input end of the fiber was measured to be approximately 75 mW using a Molectron Powermax 500D power meter. An identical 0.6 NA coupling lens was used to collect and collimate the output of the approximately 3.5-m-long fiber. In order to image the output of the fiber using a thermal camera, the output coupling lens was put in an infinite conjugate arrangement with a 500 mm focal length ZnSe lens to provide a magnification of roughly 60.



**Figure 6.4.** Experimental Apparatus to Measure the Emission Profile of Mid-Infrared Beam from a Single Mode Chalcogenide Fiber Optic Cable

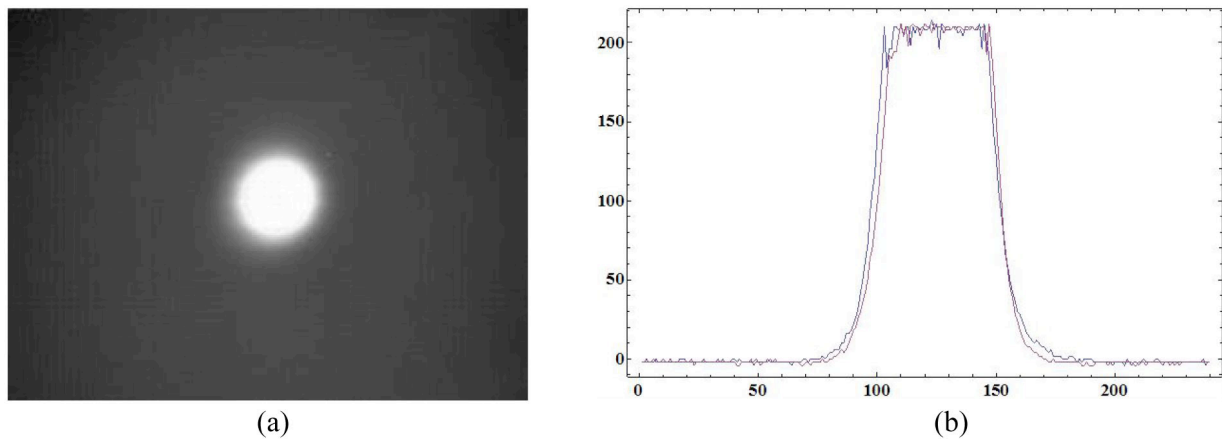
Figure 6.5(a) shows the distribution of light across the output facet demonstrating leakage from the core into the cladding and undesirable light propagation within the cladding itself. Figure 6.5(b) shows the beam profiles along the X and Y directions indicating the presence of structure outside the core region. Due to the high refractive indices of the core and cladding, minimal fiber bending can launch light into the fiber cladding. Once in the cladding, the light continues to propagate as a cladding mode. Bending or moving the fiber significantly perturbs the cladding modes, creating rapid changes in intensity pattern. These cladding modes exit the fiber facet at various angles detrimentally impacting system performance. It is therefore necessary to quench cladding modes before integration within performance optical systems.

In order to quench cladding modes, the surface of the fiber cladding had to be coated with gallium (Houizot et al. 2007) both at the entrance and the exit facets. To accomplish this, approximately 50 to 75 millimeters of the jacket was chemically stripped about 50 mm away from the facets to provide a region for the coating. Gallium in a crucible was elevated to roughly 55°C and the slag from the surface was slowly pushed aside. The stripped cladding region was then dipped into the crucible and allowed to wet by linearly translating the fiber back and forth in the crucible. The optical fiber, with the gallium-coated surfaces, was then allowed to return to room temperature before being placed back in the measurement apparatus.



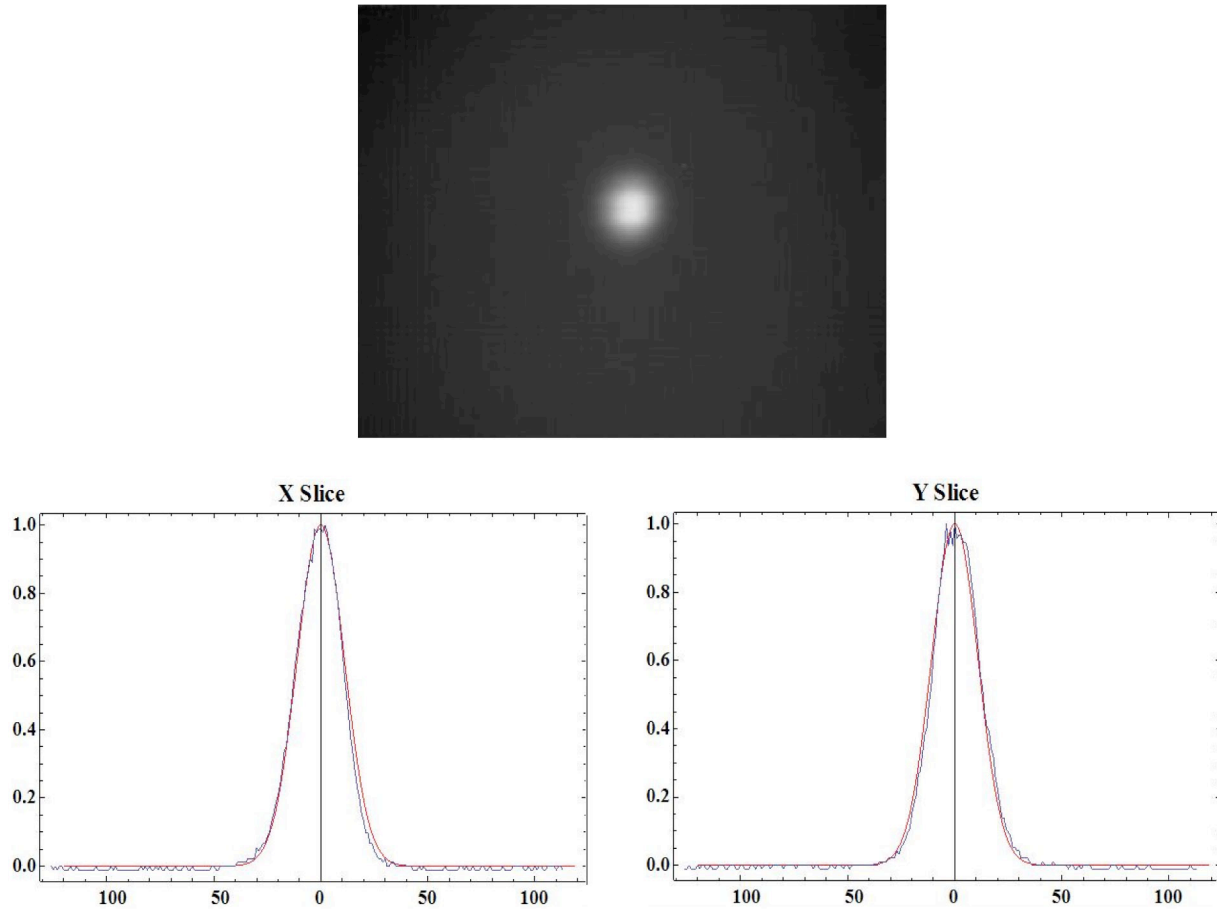
**Figure 6.5.** (a) Magnified Image of the Fiber Facet Showing Emission from the Core Along with Light Leaking from the Cladding due to the Presence of Cladding Modes; (b) Beam Profiles in Pixel Dimensions along the X (blue) and Y (red) Directions Showing the Presence of Cladding Modes

Figure 6.6(a) shows the performance of the CorActive single mode fiber with gallium applied to both ends. It can be seen that the gallium application successfully quenches the cladding modes to provide a clean output profile from the core of the fiber. Figure 6.6(b) shows the beam profile in the X and Y directions indicating that even with power sufficient to saturate the camera, the region outside the core shows no emission of light. Bending the fiber now only changes the intensity in the core region – as expected from a single mode fiber.



**Figure 6.6.** (a) Magnified Image of the Fiber Facet of a Gallium-Coated Fiber, Showing Emission Only from the Core and None from the Cladding; (b) Beam Profiles in Pixel Dimensions Along the X (blue) and Y (red) Directions Showing that the Gallium Coatings Quenched the Cladding Modes

To further characterize the beam, the power was reduced to approximately 7.5 mW at input facet to prevent pixel saturation and thereby obtain a complete emission profile. Figure 6.7 shows the circular emission profile fiber. The X and Y direction line scans of this data are also shown with a Gaussian fit that indicates single-mode emission.



**Figure 6.7.** Emission from the Output Facet of the Chalcogenide Fiber Demonstrating near Gaussian Profiles in Both X and Y Directions, Indicative of a Single-Mode Emission. The units of measurement in both dimensions are pixels.

The IRT-SE-28 fiber described in the previous section was modeled using a 3D model constructed within the RSoft Beam Propagation modeling package. Model parameters were as shown in the table below.

Parameter	Value
Core Diameter	28 $\mu\text{m} \pm 3 \mu\text{m}$
Clad Diameter	170 $\mu\text{m} \pm 5 \mu\text{m}$
Simulation Wavelength	9.2 $\mu\text{m}$
Clad index	2.7
Core $\Delta n$	0.008

Divergence data was acquired by scanning a cryogenically cooled HgCdTe detector in the far field of the fiber with the Gallium treatment described above. For this measurement, the bare output facet was clamped at the center of rotating stage on which the HgCdTe was mounted. The radial distance between the tip of the fiber and the detector was approximately 70 mm. The 9.3- $\mu\text{m}$  CO<sub>2</sub> laser beam was mechanically chopped at approximately 400 Hz before being coupled into the fiber. Power measurements using lock-in detection techniques were made in half-degree rotation increments along the hemisphere.

The measured emission profile from the chalcogenide fiber and the model output, provided in Figure 6.8, show that there is good agreement between the model and the acquired data for the far field pattern. A Gaussian model was fit to the acquired data and the  $1/e^2$  angular width was found to be  $9.23^\circ$ , which corresponds to a NA of 0.16. If we select a 1% intensity level to define beam width, the angular width is  $14.0^\circ$ , corresponding to a NA of 0.24.

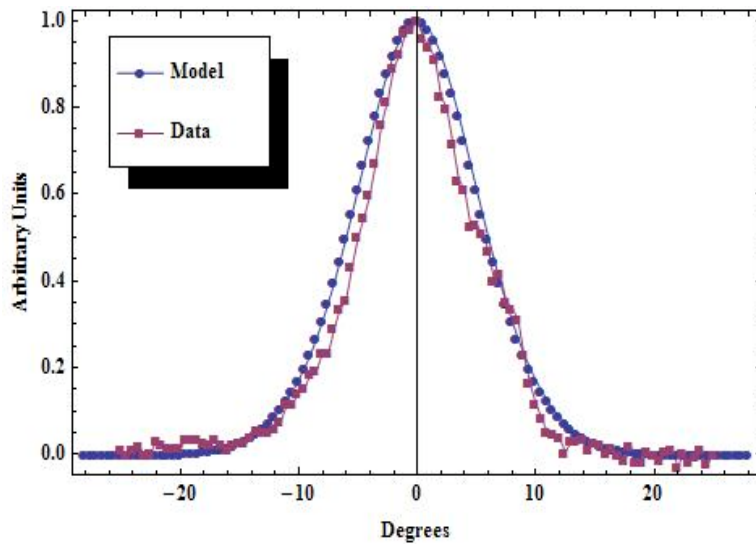


**Figure 6.8.** Modeled Data Shown Plotted with the Measured Far-Field Divergence Data, Revealing a Good Fit for the Model Assumptions Shown in the Above Table

Additionally, the model was also used to compute the mode profile for the fiber model and compared with the images shown earlier of the unsaturated fiber output after the cladding modes were stripped. If we fit a Gaussian function to the mode profile in the images shown in Figure 6.7, we find that the  $1/e^2$  width of the beam is 44.66 pixels, as shown in Figure 6.9.

A plot of the data sliced in the X-direction is shown with its Gaussian fit in Figure 6.10. The imaging system used to magnify the image at the focal plane array of the ferroelectric infrared camera was composed of two lenses used at infinite conjugates with focal lengths  $f_1$  and  $f_2$ , 8 mm and 500 mm, respectively. The magnification was thus  $f_1/f_2$ . Therefore, using the number of pixels measured, optical system magnification, and pixel pitch the beam size is found to be:

$$\text{beam size} = 44.66 \text{ pixels} \times 48.5 \frac{\mu\text{m}}{\text{pixel}} \times \frac{8}{500} = 34.66 \mu\text{m} .$$

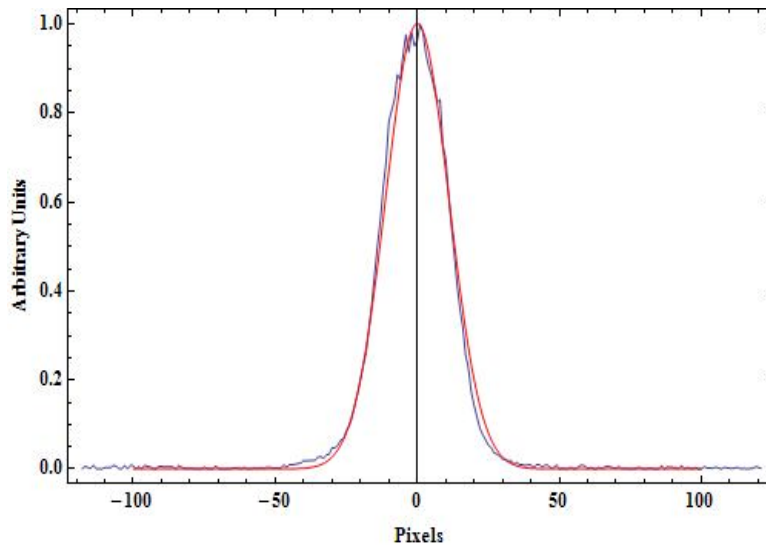


**Figure 6.9.** Image of the Mode Field Shown Earlier (blue trace) Plotted with Its Gaussian Fit (red trace). The  $1/e^2$  beam width was determined to be 44.66 pixels.

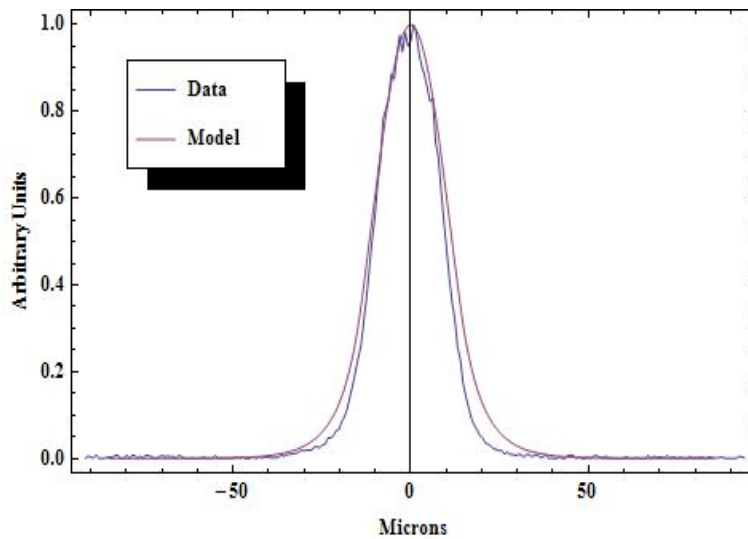


**Figure 6.10.** Model Data of the Mode Profile for the Chalcogenide Fiber Shown Compared with the Experimental Data Shown Earlier. The measured mode size is 34.66  $\mu\text{m}$ , while the modeled data was calculated to be 39.55  $\mu\text{m}$ , in relatively good agreement with experiment.

The model resulted in a beam width measurement of 39.55  $\mu\text{m}$ , which is in relatively good agreement with the experimental obtained value of 34.66  $\mu\text{m}$ .



## 7.0 Advanced Chalcogenide Photonic Components

### 7.1 Basic Waveguide Structure

Chalcogenide glasses in the As-S-Se family are promising candidates for mid-infrared photonic structures and components. A Y-junction waveguide structure was designed to provide both beam combining and splitting capability for QC laser integration. The design used the basic multi-layer structure used in previous 8.4- $\mu\text{m}$  waveguide design. Single-mode operation at the 5- $\mu\text{m}$  design wavelength was ensured by iterative optimization of both the layer thicknesses and waveguide width. The initial design and its modification for use at 5  $\mu\text{m}$  (as opposed to the original design wavelength of 8.4  $\mu\text{m}$ ) are summarized in Table 7.1.

**Table 7.1.** Device Parameters for the Original Waveguide Design and the New Design Optimized for Use at  $\lambda = 5.0 \mu\text{m}$

	8.4 $\mu\text{m}$ Design	5 $\mu\text{m}$ Design
Substrate	Si	Si
Layer 1 ( $\text{As}_2\text{S}_3$ )	4.5 $\mu\text{m}$	4.5 $\mu\text{m}$
Layer 2 ( $\text{As}_2\text{Se}_3$ )	3.8 $\mu\text{m}$	3.0 $\mu\text{m}$
Capping Layer	Air	Air
Waveguide width	5.4 $\mu\text{m}$	5.4 $\mu\text{m}$
Channel $\Delta n$	0.04	0.05

The index profile for the two layers and photomodified region are shown in Figure 7.1a. The fundamental mode was calculated using the commercial software package BeamPROP. The mode structure of the lowest order mode is shown in Figure 7.1b superimposed on the multi-layer structure.

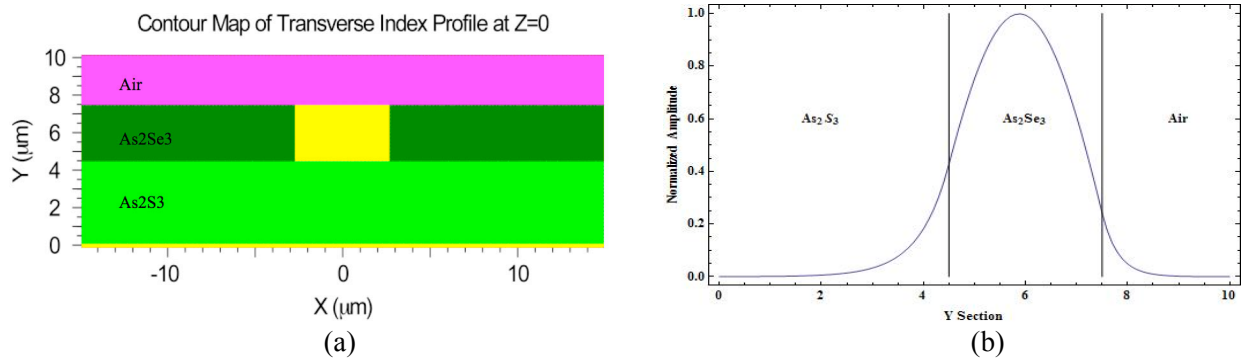


**Figure 7.1.** (a) Contour Map Depicts the Index Distribution for the Photomodified Waveguide Employing Chalcogenide Glasses for 5  $\mu\text{m}$  Operation. The yellow rectangle is the photomodified channel waveguide. (b) Cross-sectional View along the Y-Axis Shows the Mode Structure and Its Penetration into the Cladding and Capping Layers of the Y-Junction Waveguide Structure.

BeamPROP allows one to calculate the mode spectrum of all modes possible with the waveguide structure. To ensure excitation of all modes, the input launch beam, having a 3.5- $\mu\text{m}$  width in Y and 6- $\mu\text{m}$  in X, is misaligned slightly in the X-direction by an amount 1/8 the width of the waveguide. The computed mode structure is shown in Figure 7.2. As is evident from the figure, the waveguide retains the desirable single-mode operation. Finally, we model a short stretch of this waveguide totaling 1 mm to observe the propagation of the zero-order mode. Figure 7.3 shows two monitor traces, where the first trace shows the relative power and its evolution of the zero-order mode, and the second trace (Total Power) provides the integral power in the calculated field at various Z positions over the waveguide cross section.

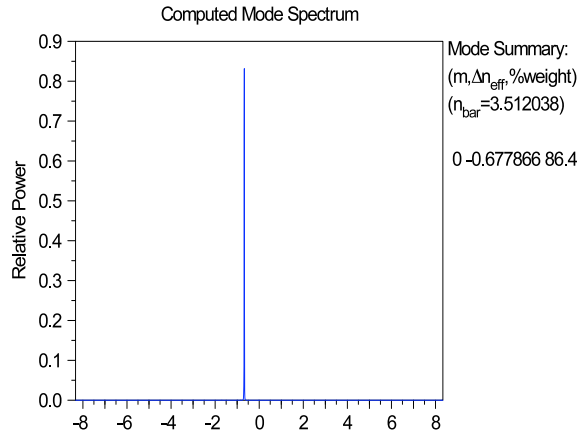


**Figure 7.2.** Computed Mode Spectrum for the Waveguide Optimized to Operate at  $\lambda= 5 \mu\text{m}$  Showing Single-Mode Operation

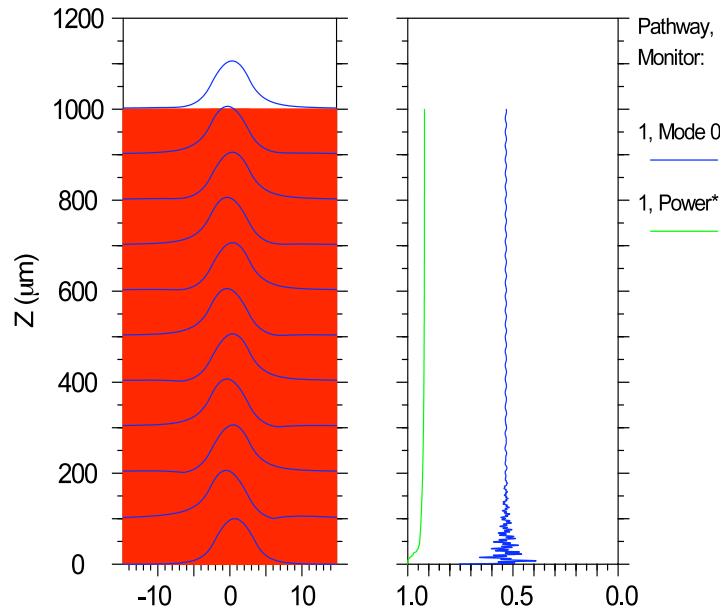


**Figure 7.3.** Evolution of the Launch Beam in the Waveguide Described Above and the Output of Two Monitors: the Power Contained in the Zero-Order Mode as well as the Total Power in the Waveguide Slab Structure

## 7.2 Y-Junction Beam Combiner Design and Modeling

A highly useful photonic device is a y-junction type beam combiner that couples two beams into two waveguide channels and outputs both beams in a single waveguide channel. The design challenge is to: (1) separate input channels enough to allow two 5.0-mm-diameter coupling lenses to be placed in close proximity to the facets, (2) minimize valuable real estate used on the silicon wafer substrate, and (3) optimize the s-bend radius of curvature to minimize loss. If the waveguide s-bend is too abrupt, the guided mode will leak into the substrate to become a radiative mode. The s-bend design curvature is restrained by the low index contrast nature of the photomodification process, because the mode is weakly confined to the waveguide and is especially subject to radiative losses.

The input arms are separated by 6 mm, and the overall length of the structure is 45 mm. Figure 7.4 shows the power in the zero-order mode in each arm for equal slab mode inputs, and monitor 3 shows the power in the final straight section, which is 1 mm in length. The design consists of arcs having a radius of curvature of 162.1 mm pieced together to complete the s-bends. Further reductions in the size (smaller radius of curvature) may require high index contrast structures (i.e., etched rib waveguides) where the propagating mode is more tightly confined.

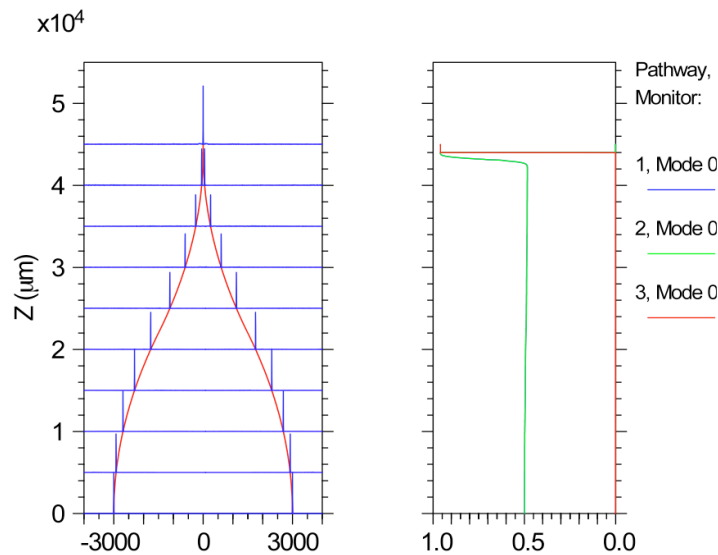


**Figure 7.4.** Final Y-Junction Waveguide Beam Combiner Consisting of Two S-bends and One Straight Section. Monitors 1 and 2 show the power in the slab mode of each arm (because they are equal, they overlap) while monitor 3 shows the combined power in the final 1-mm-long straight section.

Figure 7.5 shows the arcs that are used to construct the s-bends. The starting and ending coordinates of each arc, the s-bend radiuses of curvature, as well as the angle through which they are swept, are used to produce G-code instructions for the translation stage used in the laser waveguide writing station.

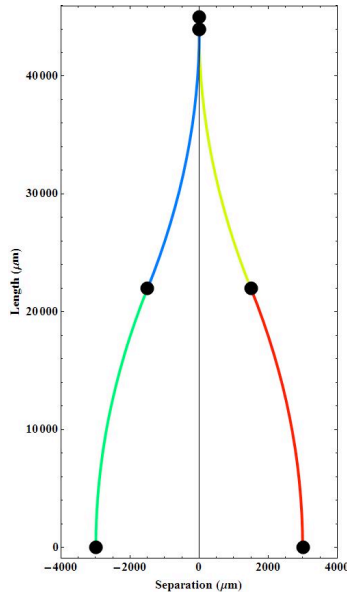


**Figure 7.5.** Coordinate System Used to Fabricate the Y-Junction Beam Combiner Described in the Text. The calculations used to produce this graph were used to generate the G-code instructions needed to program the XY stage used to pattern the waveguides in the laser waveguide writing station.

### 7.3 Device Fabrication and Testing

Material and waveguide characterization at the design wavelengths is essential for design and fabrication of optimized photonic structures and components. Of particular interest is the measurement of the photoinduced refractive index change at mid-infrared wavelengths, both for bulk and waveguide structures. We have previously measured propagation loss using the cutback method at a wavelength of  $8.4 \mu\text{m}$  on single-mode waveguides formed by direct laser writing in thin-film chalcogenide structures (Ho et al. 2006). Here we present a more detailed characterization of waveguide loss and photoinduced index change in the mid-infrared.

One method of measuring waveguide propagation loss involves analysis of the waveguide transmission when a tunable laser is propagated through a waveguide (Walker 1985). The waveguide end facets form a Fabry-Perot (FP) cavity, which generates an interference pattern as the laser is tuned in wavelength. The resulting fringe amplitude and shape depends on both the facet reflectivity and the waveguide loss. Therefore, if the facet reflectivity is known or can be calculated, the waveguide loss can be extracted from analysis of the FP fringes. Benefits of the FP loss measurement technique include a fast measurement time, especially compared to a cutback measurement, and a reduced dependence on coupling efficiency. However, the FP method does require consistent and high-quality end facet cleaves, and requires prior knowledge or assumptions of the facet reflectivity.

The transmission through the FP resonator formed by the waveguide end facets is given by an Airy transmission function. It is convenient to perform analysis using the fringe visibility  $K$ , using the maximum and minimum transmitted intensities from the fringe pattern:

$$K = \frac{T_{\max} - T_{\min}}{T_{\max} + T_{\min}}$$

From the fringe visibility, the waveguide loss is calculated via:

$$\text{Loss (dB/cm)} = -\frac{10}{L} \log \left[ \frac{1}{R} \frac{1}{K} \left( 1 - \sqrt{1 - K^2} \right) \right],$$

where R is the facet reflectivity and L is the waveguide length in cm.

We performed waveguide transmission measurements using a cryogenically cooled DFB QC laser centered at a wavelength of 8.35  $\mu\text{m}$ . The polarization of the laser was controlled using a half wave plate and linear polarizer combination to allow launching of either TE or TM modes in the waveguide. The laser was coupled in and out of the waveguide using 0.5-inch-diameter 0.8 NA germanium aspheric lenses. The output light was directed to a cryogenically cooled mercury-cadmium telluride (MCT) detector (Fermionics PV-11-1) and a custom transimpedance amplifier.

The laser wavelength was tuned by ramping the applied current from 250–720 mA at a frequency of 10 Hz. In addition, a 5-ms segment of the ramp was set to zero current to allow subtraction of detector offset. Figure 7.6a shows the applied laser current. The ramp waveform was provided to the current controller using custom National Instruments LabVIEW software and data acquisition hardware. The analog output channel driving the current ramp was updated at a rate of 200 kS/s. The detector signal was digitized using the analog input channel at a rate of 400 kS/s.

Figure 7.6b shows the detected laser intensity without the waveguide in place. The laser intensity shows a nearly linear increase with applied current except for slight roll-off at high current.

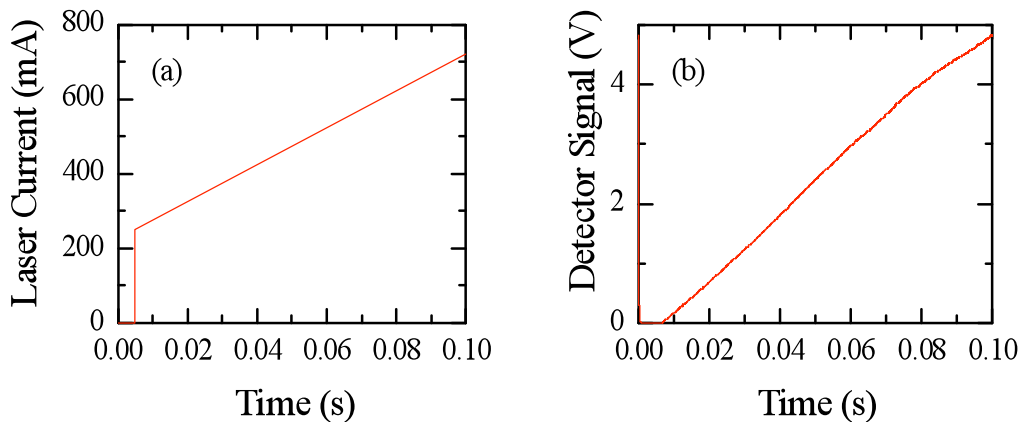


**Figure 7.6.** (a) Laser Current Ramp Waveform; (b) Detected Laser Output Intensity

The current ramp provides tuning of the laser wavelength via thermal effects. The wavelength-tuning rate was measured using a solid Ge etalon with known free spectral range of 0.0475  $\text{cm}^{-1}$ . Figure 7.7 shows the measured transmission through this etalon, normalized to the input laser intensity. The etalon peaks were located and the peak positions used to determine the wavelength tuning of the laser via

interpolation. It was determined that the overall tuning range of this laser was  $1.5 \text{ cm}^{-1}$  for the applied current ramp. The etalon results were necessary to calibrate the tuning of the laser for the waveguide refractive index measurements described below.

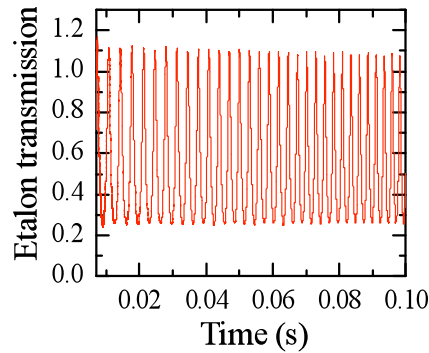


**Figure 7.7.** Transmission Measured Through Solid Ge Etalon with Free Spectral Range of  $0.0475 \text{ cm}^{-1}$ . The etalon transmission was normalized to the input laser intensity.

Chalcogenide thin films were deposited with  $3.8\text{-}\mu\text{m}$ -thick  $\text{As}_2\text{Se}_3$  and  $4.7\text{-}\mu\text{m}$ -thick  $\text{As}_2\text{S}_3$  layers. Channel waveguides were fabricated by direct laser writing using a  $633\text{-nm}$  HeNe laser focused onto the surface. For the experiments presented here, the stage was moved at a speed of  $4 \text{ mm/min}$ , and the waveguide writing laser was focused to a spot size of  $7 \mu\text{m}$  using an aspheric lens (LightPath Technologies, part number 350220). A series of waveguides were patterned on the film in which the writing laser power was varied from  $0.05\text{--}5 \text{ mW}$  to alter the effective writing dose, and thereby vary the photoinduced refractive index change. The film section containing the waveguides was cleaved to provide perpendicular end facets suitable for waveguide transmission measurements. Figure 7.8 shows an example of the detected laser signal transmitted through one of the waveguides written at  $1\text{-mW}$  power, normalized to the input intensity. The FP fringes are clearly visible as are the differences between TE and TM modes.

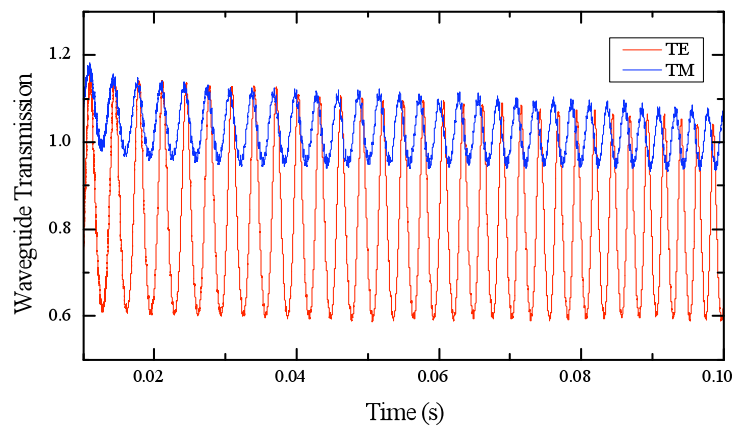
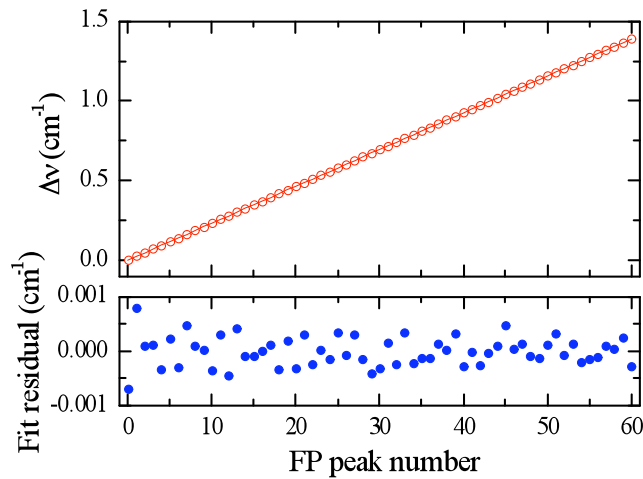


**Figure 7.8.** Transmission Measured Through Waveguide Written with  $1\text{-mW}$  Power, Normalized to the Input Laser Intensity for TE (red) and TM (blue) Polarization

Straight waveguides were cleaved into sections with a length of 3.80 cm, for which a series of over 30 FP fringes were observed. The etalon peaks were located and the mean fringe separation was used to calculate the group refractive index, based on the wavelength tuning calibration of the QC laser. The amplitude of the fringes was used to compute the fringe visibility, which in turn was used to calculate the waveguide loss. The location and amplitude of the fringes were determined using an analysis routine written in LabVIEW. In addition to the FP fringes from the waveguide, the data also contained small amplitude higher-frequency and lower-frequency fringes of unknown origin. These fringes were removed by using a 3<sup>rd</sup> order Savitsky-Golay filter on the data. From the fringe separation  $\Delta v$ , the waveguide group effective index  $N_{\text{eff}}$  can be determined via the relationship

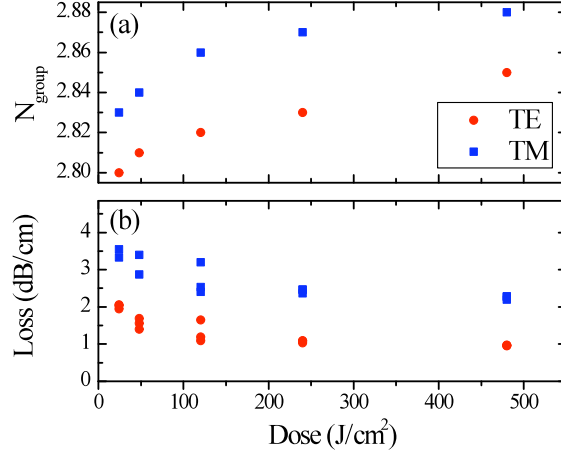
$$\Delta \bar{v} = \frac{1}{2N_{\text{eff}}L}$$

Figure 7.9 shows the location of the peaks and valleys of the fringes for one waveguide, calibrated to wavenumber. A linear fit was performed using the data, and the slope used to calculate the effective index.



**Figure 7.9.** Position of WG Transmission FP Fringes and Linear Fit Used to Determine  $N_{\text{eff}}$ . The fit residuals are shown in the lower graph.

The fringe amplitudes were used to calculate the fringe visibility  $K$ , as described above. This value was in turn used to calculate the waveguide loss. The facet reflectivity was calculated using finite-difference time-domain simulations of the waveguide structure, resulting in  $R = 0.35$  for TE and  $R = 0.26$  for TM polarization. Note that these values are both larger than the reflectivity of 0.22 calculated using the Fresnel formula with the refractive index of the waveguide core. Figure 7.10 shows the measured group refractive index and waveguide loss for both TE and TM propagation, as a function of peak writing dose. Three waveguides were characterized for each writing dose.



**Figure 7.10.** Measured Group Refractive Index (top) and Waveguide Loss Versus Writing Laser Dose for TE (circles) and TM (squares) Polarization (bottom)

The measured group refractive index increases with writing laser dose as expected for an increasing refractive index of the waveguide core, and the leveling off at higher doses indicates that the glass is approaching saturation of its photoinduced index change. The measured group indices for the TM modes were higher than the TE modes, which is consistent with modeling results discussed below. Losses as low as 1.0 dB/cm were measured for the highest dose and the TE propagation mode. At doses above 500 J/cm<sup>2</sup> (not shown in Figure 7.10) significant physical modification of the waveguide surface was observed and the waveguides ceased supporting single-mode propagation.

The group index of refraction is related to the modal effective index via the relationship

$$N_{group} = N_{eff} - \lambda \frac{dN_{eff}}{d\lambda}$$

The modal effective index and its dispersion were calculated using the BeamPROP software package with the waveguide modeled as a step-index structure. Figure 7.11 shows the calculated modal effective index and group index for the waveguide structure as a function of photoinduced index change of the waveguide core  $\Delta n$ . Although it is difficult to match the absolute index values of the experiment and model due to uncertainties in both film indices and profile of the photomodified core region, the calculated results verify several experimental observations. The calculations confirm that for these waveguide structures, the TM group index is expected to be higher than the TE group index, and both values are larger than the waveguide core material index and modal effective indices. Furthermore, the model indicates that over this range of index photomodification, the change in group index is linear with a slope of 1.1. Therefore, we can infer that measured change in group index results from a corresponding change in the waveguide core index of slightly smaller magnitude.

In summary, we have fabricated laser-written single-mode channel waveguides in chalcogenide glass thin films and characterized the propagation loss and group refractive index using a QC laser emitting at a wavelength of 8.35  $\mu\text{m}$ . Modeling of the waveguide structure confirms the experimentally observed behavior of the group refractive index. These measurements of waveguide and material properties at mid-infrared wavelengths will allow design and fabrication of photonic structures optimized for mid-infrared operation.

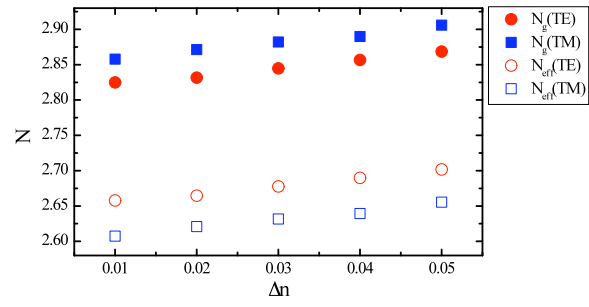


**Figure 7.11.** Calculated Group Refractive Index (solid points) and Waveguide Effective Index (open points) Versus Photoinduced Index Change of the Waveguide Core for TE (circles) and TM (squares) Modes



## 8.0 Mid-Infrared Refractive Index Measurement of Chalcogenide Glass Materials Using Prism Coupling

The design of integrated optical elements requires a precise knowledge of their refractive index, as well as the influence of processing steps, such as the post-deposition annealing of thin films. Unfortunately, many of the currently available techniques for measurement of the refractive index of films offer inadequate precision, or cannot access the mid-infrared spectral region, where many of the applications of these materials are desired.

### 8.1 Prism Coupler Method

Techniques commonly used for the measurement of the refractive index of thin materials include modeling of spectroscopic data (transmission or reflection), various ellipsometric techniques, and prism coupling. The prism-coupling technique offers high-resolution, simple data analysis, and is self-referencing. Additionally, this technique can be used to measure bulk materials as well as films, and no specific sample preparation is generally necessary, other than the measured surface must be reasonably flat and free from contaminants. This makes the prism-coupling technique very attractive. However, to date, commercial systems have been designed to function only over the visible and near-infrared spectral regions. In order to address this shortcoming, a commercial prism coupler instrument (Metricon, model 2010) has been modified to include the ability to perform measurements over the mid-infrared region, covering a wavelength range using discrete laser wavelengths from 0.6328 to 10.6  $\mu\text{m}$ . In this study we present the system design and modification, as well address the data analysis problems specific to its use in the mid-infrared. We further show the effects of film deposition and annealing on the refractive index of  $\text{As}_2\text{Se}_3$  glass, and on its photoresponse under band gap illumination.

The prism coupling technique functions by pressing a sample to the hypotenuse of an isosceles prism fabricated from a high-index material. The prism and sample are rotated relative to a collimated light source, typically a HeNe laser, and the intensity that is transmitted through the prism is monitored as a function of incident angle, as shown in Figure 8.1.

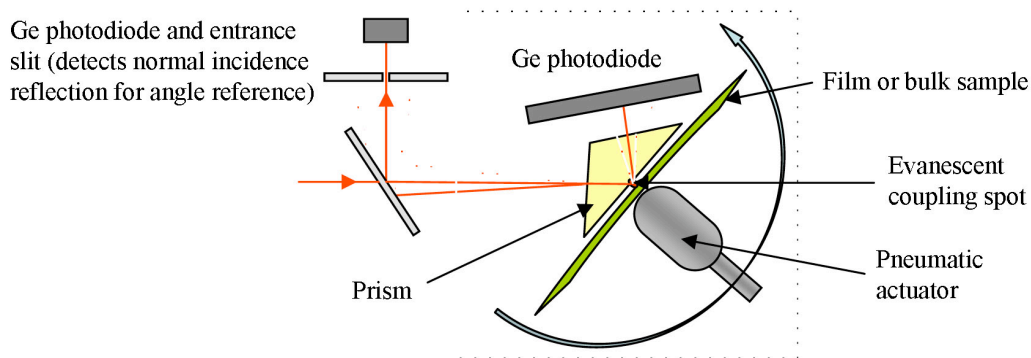


**Figure 8.1.** Metricon Model 2010 Prism Coupler Arrangement

For a sufficiently flat surface, light reflected within the prism can couple into the sample through the evanescent field at an angle that is dependent on the refractive indices of the sample and prism. Additionally, the angle of the prism is referenced by detecting the back-reflection of the laser from the input face of the prism. This has the advantage of removing the effects of any change in prism alignment between measurements. The intensity of the transmitted light as a function of angle for bulk and film samples is simulated in Figure 8.2.

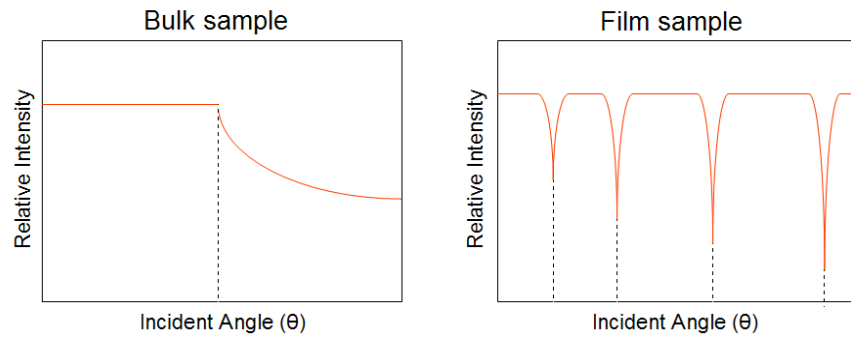


**Figure 8.2.** Simulated Output Intensity as a Function of Incident Angle for Bulk Samples (left) and Thin Films (right)

As can be seen for a bulk sample a single knee in the intensity plot is found, and the refractive index is calculated from the corresponding angle. For a film sample, a series of dips is found. The film refractive index and thickness can be calculated if the indices of the prism and substrate are known. It should be noted that absolute intensity is not significant for either measurement. Furthermore, the calculation of thickness and index in a film sample requires at least two modes to be observed, which in practice requires a film thickness of approximately one-half of the measurement wavelength or greater. Due to the use of monochromatic light source, this technique cannot generally provide information on the wavelength dispersion of the refractive index.

## 8.2 Mid-Infrared Apparatus

In order to allow measurement at longer wavelengths, several modifications to the commercial instrument configuration are necessary, including incorporation of a mid-infrared detector and additional laser sources and a coupling prism. For chalcogenide glasses, their high transparency in the infrared leads to applications in mid-infrared photonics and sensing. This makes the ability to precisely measure the mid-infrared refractive index of chalcogenide bulk or film materials attractive. In order to accommodate the transparency range of these glasses, we have expanded the capabilities of the instrument to cover the visible to mid-infrared range. The configuration of the instrument is shown in Figure 8.3.

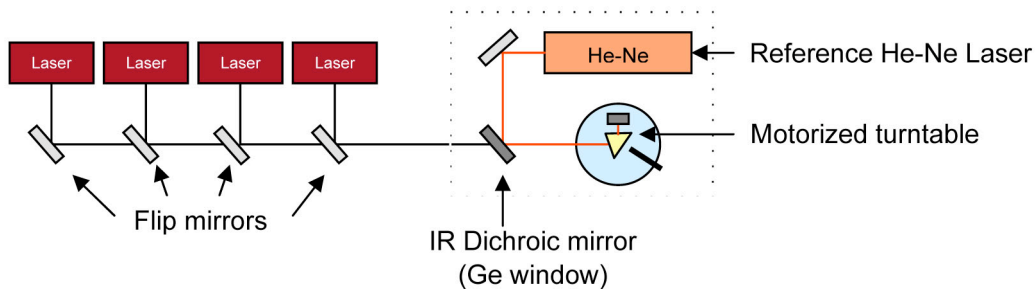


**Figure 8.3.** Optical Configuration of the Prism Coupler System, Modified for Operation in the Mid-Infrared Spectral Region

The laser sources used in this study include the 632.8-nm HeNe laser, which is equipped with the commercial configuration as well as a 1547-nm telecom fiber laser, both of which may be used with the standard rutile prism and germanium detector. Additionally, a 3.391- $\mu\text{m}$  HeNe laser and a 5.348- $\mu\text{m}$  DFB QC laser have been added, as well as a tunable  $\text{CO}_2$  laser operating over the range of 9.3 to 10.6  $\mu\text{m}$ . A HeNe laser is used as a reference; therefore, it is necessary to combine the visible and infrared beams. In order to accomplish this, a Ge window is used to act as a dichroic mirror, reflecting visible and near-infrared wavelengths and passing those in the mid-infrared. It should be noted, therefore, that any discrepancy in the alignments of these various lasers will result in an inaccuracy in the refractive index measurement. Precise alignment was achieved by first placing an aperture in front of the Ge window, then imaging all of the lasers onto an pyroelectric camera (Electrophysics Corp., model PV320L). The use of mid-infrared wavelengths also requires substitution of the prism material and the detector.

A Ge prism is used for measuring infrared glass having index of refraction from 3.5 to 2.6. A gallium phosphide (GaP) is used for lower index glasses in the range of 2.7 to 1.6. Both of these materials are transparent over the mid-infrared range (2.0 to 10.8  $\mu\text{m}$ ) used in this study; however, the GaP prism has an absorption band gap that extends into the visible, conveniently allowing measurement over the entire range of 0.6–10.6  $\mu\text{m}$  with a single prism.

MCT is a common detector that can be used over the entire 2.2- $\mu\text{m}$  to 10.6- $\mu\text{m}$  wavelength range. However, these detectors must generally be cryogenically cooled in order to reduce noise from thermally excited electrons. Due to the small space in which the detector must be placed, cryogenically cooled devices are not practicable. A relatively new detector material, mercury-cadmium-zinc-telluride (MCZT), can operate over a similar wavelength range as MCT, but has improved thermal and electrical properties, making it capable of detection with lower noise at room temperature. For this reason, a MCZT photovoltaic detector (Vigo Systems, model PVM-10.6) has been used. In order to improve the signal-to-noise ratio, the laser sources are optically chopped at 1 kHz. The raw signal from the detector was first amplified (Stanford Research, model SR570) and then the signal was recovered using a lock-in amplifier (Princeton Applied Research, model 5208). The dc output signal was then applied to the detector input of the Metricon instrument controller. Due to wide range of angles scanned during the measurement ( $\sim 60^\circ$ ) and to the small size of the MCZT detector (3 mm  $\times$  4 mm), it is necessary to place the detector at a small distance (0.1 mm) from the output face of the prism to prevent the refracted beam from walking off the detector. To satisfy this requirement, the MCZT detector TO-9 housing was removed. Our evaluation of the new detector configuration demonstrated detection with low noise at the same scan rate and angular range provided by the factory-configured Ge photodiode detector.

### 8.3 Mid-Infrared Index Measurements

The Metricon prism coupler was originally designed to measure index of refraction from visible to near-infrared wavelengths. The design team never envisioned using this instrument at wavelengths longer than 1.6  $\mu\text{m}$ . As a consequence, the analysis software is not capable of correctly calculating the film thickness using measurements at wavelengths longer than 1.6  $\mu\text{m}$ . Therefore, a separate program was written to perform the required analysis. The analysis of the data for film thickness and index is accomplished by recording the intensity values as a function of incident angle, and determining the location of the minima observed in the signal. The effective index of the guided mode ( $N_m$ ) corresponding to the each minimum is determined from the incident angle of the mode ( $\theta_m$ ), the prism cut angle ( $\epsilon$ ), and the prism refractive index ( $n_p$ ) using the following relation:

$$N_m = \sin \theta_m \cos \epsilon + \left( n_p^2 - \sin^2 \theta_m \right)^{1/2} \sin \epsilon$$

The film refractive index ( $n_f$ ) and thickness ( $W$ ), are found to lie at discrete positions where the mode order ( $m$ ) has an integer value and follows the relation:

$$k_{x_f} W + \phi_{f_s} + \phi_{f_i} = m\pi$$

where:

$$k_{x_f} = \left( \frac{2\pi}{\lambda} \right) \sqrt{n_f^2 - N_m^2} \quad \text{and} \quad \phi_{f_i} = -\tan^{-1} \left( \frac{N_m^2 - n_i^2}{n_f^2 - N_m^2} \right).$$

The values  $\phi_{f_s}$  and  $\phi_{f_i}$  are the respective phase shifts caused by internal reflection of the optical wave from the top surface of the film or the substrate interface, and  $n_t$  and  $n_s$  (each substituted for the variable  $n_i$ ) therefore correspond to the refractive index of air and the substrate respectively.

The challenge then is to find a single value of  $n_f$  and  $W$  that solves the set of transcendental equations describing the position of the intensity minima. In order accomplish this we utilize a linear regression method (Kirsch 1981). An initial guess value for the refractive index is calculated from the position of the first two minima in order of increasing mode index ( $N_m$ ) using the equation:

$$n_f = \sqrt{\frac{4(N_0^2 - N_1^2)}{3}}$$

Once the estimated film index is known, approximate values of the two phase shifts,  $\phi_{f_s}$  and  $\phi_{f_i}$ , may be calculated. The following relationship between effective mode index ( $N_m$ ) and mode order number ( $m$ ) may then be fit using linear regression through the following relation.

$$y_m = C_1 x_m + C_2$$

where:

$$y_m = N_m^2$$

$$C_1 = -(\lambda/2W)^2$$

$$C_2 = n_f^2$$

$$x_m = \left[ m - \frac{\phi_{fs} + \phi_{ft}}{\pi} \right]^2$$

The refractive index may then be calculated from the  $x_m$  intercept, and the thickness from the slope of the line. The film index derived from regression is then used to improve the initial estimates of the values of the  $\phi_{fs}$  and  $\phi_{ft}$  phase shifts and the regression is performed again. This iterative refinement is continued until the change in  $n_f$  between each iteration is significantly less than the expected precision of the index measurement, which is  $1 \times 10^{-5}$  refractive index units (RIU) for our instrument.

Thin  $\text{As}_2\text{S}_3$  and  $\text{As}_2\text{Se}_3$  film layers were deposited using thermal evaporation of commercial glass materials AMTIR2 and AMTIR6, respectively (Amorphous Materials Inc.). The target consisted of 5.5 g of ground bulk  $\text{As}_2\text{S}_3$  and 7.7 g of ground bulk  $\text{As}_2\text{Se}_3$  glass, placed in a fused silica crucible. The substrate was a non-oxidized 4-inch Si wafer (Silicon Quest), and deposition was carried out using a deposition process described in a prior report. A 4.5- $\mu\text{m}$  under-cladding of  $\text{As}_2\text{S}_3$  was first deposited, followed immediately by deposition of a 7.6- $\mu\text{m}$   $\text{As}_2\text{Se}_3$  layer. The temperature of the substrate and stage was not controlled during deposition. Following deposition, one half of the film sample was annealed at 170°C for a period of 3 hours and at a heating and cooling rate of 1°C/min. The refractive index of the parent bulk glass and films has been measured in the 0.6328- $\mu\text{m}$  to 10.591- $\mu\text{m}$  region and is shown in Figure 8.4.

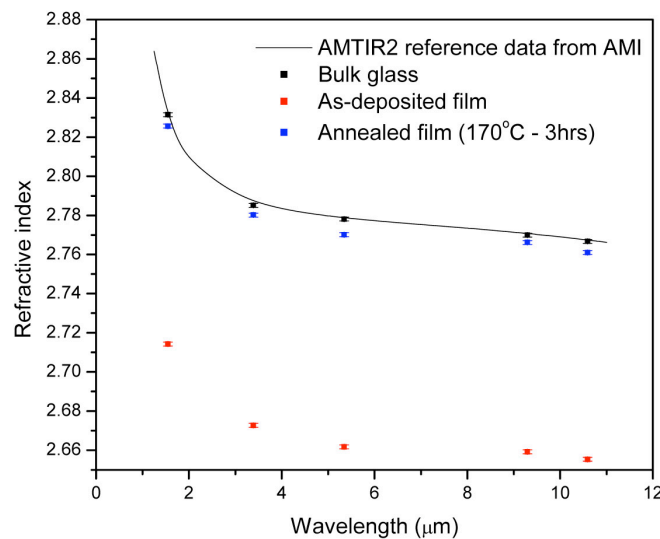


**Figure 8.4.** Measured Refractive Index Dispersion of Bulk AMTIR2, Compared with Reference Data for AMI, and Index Dispersions for As-Deposited and Annealed Films

It can be seen from the figure that the refractive index of the bulk glass is in good agreement with the reference data, showing the high level of accuracy achievable using the prism-coupling method. The refractive index of the annealed film is also found to be close to that of the bulk glass, while that of the as-deposited film is significantly lower. This behavior is often observed in chalcogenide thin films. It is well known that the high cooling rate of the vapor, as it condenses into the solid glass film during thermal evaporation, leads to a film with a structure that is far from equilibrium. The glassy film generally possesses lower density compared to the parent bulk glass, and therefore, a correspondingly lower refractive index. Annealing the glass film near its glass transition temperature results in structural relaxation. This relaxation leads to a higher density glass structure that is closer to equilibrium, and a refractive index that is similar to the corresponding bulk glass. Therefore, by using the prism-coupling technique, it is possible to accurately judge the effectiveness of the annealing process by examining how similar the refractive index of the annealed film is compared to bulk glass.

## 8.4 Photomodification Studies

To examine the possibility of precisely measuring the mid-infrared refractive index change in chalcogenide thin films after band gap irradiation, thin films of  $\text{As}_2\text{Se}_3$  (7- $\mu\text{m}$ ) were deposited from AMTIR2 commercial glass using thermal evaporation. Relatively thick films are used because the prism-coupling measurement requires film thickness at least one-half the characterization wavelength. The as-deposited thin films were then exposed to HeNe laser irradiation using a spot size of 8 mm at an irradiance of  $56 \text{ mW/cm}^2$  for varying periods between 8 and 32 hours. The refractive index of the films as a function of wavelength for varying dose is shown in Figure 8.5.

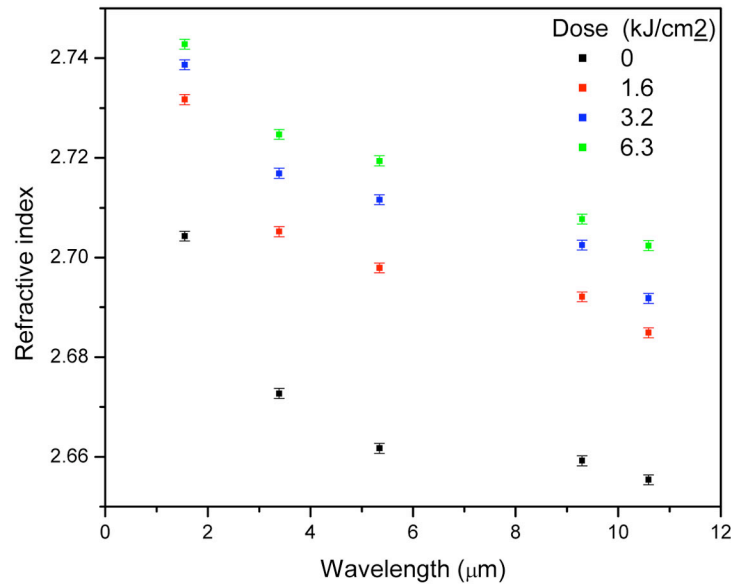


**Figure 8.5.** Refractive Index Data of the  $\text{As}_2\text{Se}_3$  Film Measured Between 3.3 to 10.6  $\mu\text{m}$  as a Function of Dose

The film refractive index increases upon exposure, but appears to begin to saturate at higher doses as shown in Figure 8.6. Additionally, the index change magnitude is not constant as a function of wavelength. The refractive index increases by up to 0.06 RIU at 5.348  $\mu\text{m}$ , which is the largest change, while the smallest change, only 0.04 RIU occurs at a wavelength of 1.547  $\mu\text{m}$ . The inconsistency of the RIU magnitude could be attributed to variation in laser polarization, which was not accounted for during these measurements. In addition, the Ge prism used in these index measurements has a rather large thermal refractive index coefficient,  $dN/dT$ , of approximately 400 ( $10^{-6}/^{\circ}\text{C}$ ). Room temperature fluctuations on the order of  $1^{\circ}\text{C}$  begin to produce apparent index measurement variations at the resolution of the instrument. To remedy this issue, we plan to install a thin foil heater to stabilize the Ge prism temperature just above ambient room temperature.

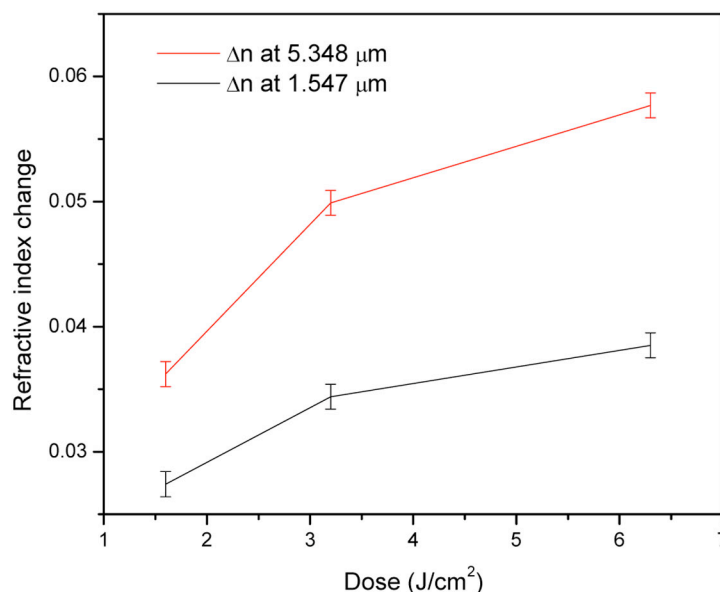


**Figure 8.6.** Refractive Index of the  $\text{As}_2\text{Se}_3$  Film at 1.547 and 5.348  $\mu\text{m}$  as a Function of Dose

While no literature values for photoinduced  $\Delta n$  have been found for mid-infrared wavelengths, similar magnitudes for  $\Delta n$  under HeNe laser irradiation of 1–2% have been previously reported for near-infrared wavelengths (van Popta et al. 2002; Robinson et al. 2003). It should be noted, however, that these thick films displayed relatively poor adhesion, which led to film delamination during repeated prism-coupling measurements. This issue prevented measurement on the same film location before and after irradiation. While the refractive index of the film was found to be homogenous across the surface of the wafer, a slight inhomogeneity in the film thickness (2%) was observed. Therefore, values for photoinduced thickness changes (e.g., photoexpansion) could not be accurately determined for these samples and are not reported.

Finally, an annealed film was exposed to identical conditions as those used for the as-deposited films. The refractive index dispersion of the annealed film is shown in Figure 8.7.

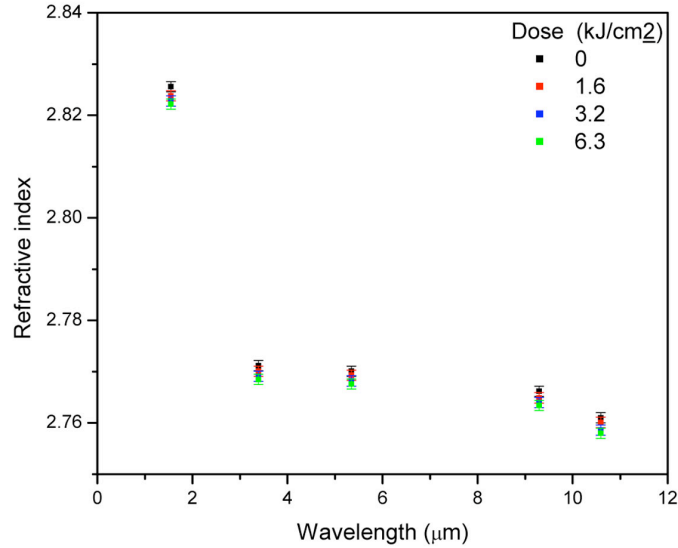


**Figure 8.7.** Refractive Index Data of the Annealed Film as a Function of Laser Dose

One can see from Figure 8.7 that the photoinduced refractive index change in the annealed film is significantly smaller compared to the as-deposited film study. Additionally, the sign has changed, showing a slight decrease of refractive index as dose increases. The refractive index was found to decrease uniformly by 0.003 RIU at all wavelengths, with no significant saturation observed. This result is unexpected, and investigation to confirm this result is still ongoing. In addition, these results contradict our previous study of band gap laser written waveguides in annealed films. Here we successfully demonstrated low-loss waveguides at 8.3- $\mu\text{m}$  wavelength. In this case, if the laser photomodification resulted in an index decrease, a guided mode condition in the core would not be possible. It is possible that small variations in the deposition and annealing processing can produce variability in the initial energy of the glassy film structure, leading to unexpected and potentially undesirable photorefractive behaviors. These results further demonstrate the importance of optical metrology tools, like prism coupling, at mid-infrared wavelengths.

These results suggest that for effective laser writing of waveguide structures in  $\text{As}_2\text{Se}_3$  thin films, exposure of as-deposited films, rather than annealed films, will result in a larger induced index change producing waveguides with better confinement. It is also shown that knowledge of the induced index change at visible wavelengths is not sufficient to predict the index change at mid-infrared wavelengths.

It has been shown that the refractive index of chalcogenide glasses can be measured across the visible, near, and mid-infrared spectral range using the prism-coupling technique. Additionally, the technique was shown to have significantly improved accuracy as compared to spectroscopic and ellipsometric methods, with an experimental error of 0.0005 RIU for bulk glasses and 0.001 RIU for thin films. The ability to precisely measure the refractive index change, which is induced during film processing steps such as deposition and annealing, as well as the photoinduced index change, which occurs upon laser irradiation, of chalcogenide films has also been demonstrated. Access to precise refractive index values across the entire transparency region of these glasses will allow the optimization of the device design and processing steps which is key for the development of high-performance, integrated infrared photonics and sensing applications.

## 9.0 Summary

During FY 2008, PNNL's Infrared Photonics research team continued developing the science and technology needed to meet the demand for lighter, more compact, and integrated mid-infrared remote sensing system designs.

Improvements in PNNL's chalcogenide glass thin-film deposition facility were made, including development of an ion gun chamber for substrate cleaning prior to deposition and installation of a three-gun magnetron sputtering system for various metal and dielectric thin film deposition. New channel waveguide designs were produced including y-junction beam combiners and waveguides for propagation wavelengths near 5  $\mu\text{m}$ . These devices were all fabricated using direct-laser writing exploiting the photomodification properties of chalcogenide glasses. The performance of the fabricated waveguides was characterized using a waveguide transmission measurement that incorporated a mid-infrared tunable laser. Custom asphere lenses were designed and fabricated to couple in and out of these channel waveguides.

A prism-coupling technique was developed to measure the refractive index of chalcogenide glasses across the visible, near, and mid-infrared spectral range. This instrumentation provides the ability to precisely measure refractive index change due to thin-film processing and/or laser-written photomodification in chalcogenide glass. Precise index measurements now allow for accurate device modeling and improved fabrication control to produce novel photonic structures specifically optimized for mid-infrared applications.

PNNL also made significant progress in processing and characterizing commercially available chalcogenide fiber optics. Due to the frangible nature of chalcogenide fiber optics, standard fiber optic tools and processes developed for silica fibers are not immediately applicable. Towards this, we have successfully developed repeatable processes to strip the jacket, produce straight and angle cleave fibers, and polish connectorized fiber facets. Our measurements of commercially available chalcogenide fibers indicated the need to quench cladding modes which was successfully accomplished by applying a coating of gallium metal on the cladding near both input and output facets. Upon successfully quenching the cladding modes, single-mode emission with a near-Gaussian profile was obtained from these commercial fibers.

PNNL continued to make significant progress towards the development of an integrated QC laser transmitter housed in an HHL package. The integrated QC laser transmitter design was characterized using a 5.3- $\mu\text{m}$  DFB QC laser. The C-mount QC laser was mounted in the HHL package along with custom-designed germanium asphere collimation lens optimized for 5- $\mu\text{m}$  wavelength. These lenses exhibit diffraction-limited performance with tolerance to misalignment that occurs in the course of integrating optomechanical elements. The emission wavelength versus temperature and injection current were characterized as well as the long-term frequency drift. Our results show that the HHL package QC laser transmitter provides a stable laser source for laser-based sensing platforms.



## 10.0 References

- Allen PJ, BR Johnson, RT Baran, JNC Anheier, SK Sundaram, MH Engelhard and BT Broocks. 2006. "Surface Degradation of As<sub>2</sub>S<sub>3</sub> Thin Films." *Phys. Chem. Glasses* **47**(6):681-687.
- Anheier NC, Jr., PJ Allen, BE Bernacki, N Ho, K Krishnaswami, HA Qiao and JF Schultz. 2006. *FY 2006 Infrared Photonics Final Report*. PNNL-16319. Pacific Northwest National Laboratory, Richland, WA.
- Anheier NC, Jr., PJ Allen, N Ho, K Krishnaswami, BR Johnson, SK Sundaram, BJ Riley, JE Martinez, HA Qiao and JF Schultz. 2005. *FY 2005 Infrared Photonics Final Report*. PNNL-15581. Pacific Northwest National Laboratory, Richland, WA.
- Anheier NC, Jr., PJ Allen, PE Keller, WD Bennett, PM Martin, BR Johnson, SK Sundaram, BJ Riley, JE Martinez, HA Qiao and JF Schultz. 2004. *FY 2004 Infrared Photonics Final Report*. PNNL-15209. Pacific Northwest National Laboratory, Richland, WA.
- Anheier NC, Jr., BE Bernacki, BK Hatchell, N Ho, K Krishnaswami and HA Qiao. 2007. *FY 2007 Infrared Photonics Final Report*. PNNL-17392, Limited Distribution. Pacific Northwest National Laboratory, Richland, WA.
- Bernacki BE, K Krishnaswami, NC Anheier, Jr. and BD Cannon. 2008a. "Design and Fabrication of Efficient Collimation and Focusing Optics for mid-IR Quantum Cascade Lasers." In *Laser Source Technology for Defense and Security IV* Vol. 6952, pp. 69520H-9. March 17, 2008, Orlando, Florida. eds: M Dubinskii and GL Wood. SPIE, Bellingham, Washington.
- Bernacki BE, K Krishnaswami, NC Anheier, Jr. and BD Cannon. 2008b. "Design and Fabrication of Efficient Collimation and Focusing Optics for mid-IR Quantum Cascade Lasers." In *Laser Source Technology for Defense and Security IV* 6952, p. 69520H. March 17, 2008, Orlando, Florida. eds: M Dubinskii and GL Wood. SPIE, Bellingham, Washington.
- Carlie NA, NC Anheier, Jr., A Qiao, MA Phillips, BE Bernacki, L Petit and K Richardson. 2008. "Measurement of the Refractive Index of Chalcogenide Thin Films Using Prism Coupling in the Near and Mid-Infrared." *8th Pacific Rim Conference on Ceramic and Glass Technology*. Vancouver, BC, Canada. Abstract submitted.
- Chia-Pin C, GL Solbrekken and YD Chung. 1997. "Thermal Modeling of Grease-type Interface Material in PPGA Application." In *Proceedings of Thirteenth Annual IEEE Semiconductor Thermal Measurement and Management Symposium, SEMI-THERM XIII*, pp. 57-63. January 28-30, 1997, Austin, Texas. IEEE, Piscataway, New Jersey.
- Ho N, MC Phillips, A Qiao, PJ Allen, K Krishnaswami, BJ Riley, TL Myers and NC Anheier. 2006. "Single-Mode Low-Loss Chalcogenide Glass Waveguides for the Mid-Infrared." *Optic. Lett.* **31**(12):1860-1862.
- Houizot P, C Boussard-Plédel, AJ Faber, LK Cheng, B Bureau, PA Van Nijnatten, WLM Gielesen, J Pereira do Carmo and J Lucas. 2007. "Infrared Single Mode Chalcogenide Glass Fiber for Space." *Optic. Express* **15**(19):12529-12538.

- Kirsch ST. 1981. "Determining the Refractive Index and Thickness of Thin Films from Prism Coupler Measurements." *Appl. Optic* **20**(12):2085-2089.
- Krishnaswami K, BE Bernacki, BD Cannon, N Ho and NC Anheier, Jr. 2008a. "Emission and Propagation Properties of Mid-Infrared Quantum Cascade Lasers`." *IEEE Photon. Tech. Lett.* **20**(4):306-308.
- Krishnaswami K, BE Bernacki, BD Cannon, N Ho and NC Anheier, Jr. 2008b. "Emission and Propagation Properties of Mid-Infrared Quantum Cascade Lasers`." *IEEE Photon. Tech. Lett.* **20**:306-308.
- Krishnaswami K, BE Bernacki, N Ho, PJ Allen and JNC Anheier. 2008c. "Lateral Shearing Interferometer for Measuring Photoinduced Refractive Index Changes in Amorphous As<sub>2</sub>S<sub>3</sub>." *Rev. Sci. Instrum.* **79**(9):095101.
- O'Hanlon JF. 2003. *A User's Guide to Vacuum Technology, Third Edition*. John Wiley & Sons, Inc., Hoboken, New Jersey.
- Rao VV, K Bapurao, J Nagaraju and MV Krishna Murthy. 2004. "Instrumentation to Measure Thermal Contact Resistance." *Meas. Sci. Technol.* **15**:275-278.
- Robinson TG, RG DeCorby, JN McMullin, CJ Haugen, SO Kasap and D Tonchev. 2003. "Strong Bragg Gratings Photoinduced by 633-nm Illumination in Evaporated As<sub>2</sub>Se<sub>3</sub> Thin Films." *Optic. Lett.* **28**(6):459-461.
- van Popta A, R DeCorby, C Haugen, T Robinson, J McMullin, D Tonchev and S Kasap. 2002. "Photoinduced Refractive Index Change in As<sub>2</sub>Se<sub>3</sub> by 63nm Illumination." *Optic. Express* **10**(15):639-644.
- Walker RG. 1985. "Simple and Accurate Loss Measurement Technique for Semiconductor Optical Waveguides." *Electron. Lett.* **21**(13):581-583.

## **Appendix A**

### **Papers and Presentations Generated by This Project**



# Appendix A

## Papers and Presentations Generated by This Project

### A.1 ITAS Photonics Project Papers

Anheier NC, BR Johnson and SK Sundaram. 2004. "Laser Writing in Arsenic Trisulfide Glass." In *Optoelectronic Materials and Devices Volume 1, 2004, Non-Crystalline Materials for Optoelectronics*. eds: G Lucovsky and M Popescu. INOE Publishing House, Bucharest. Invited book chapter.

Anheier JNC, PJ Allen and TL Myers. 2004. "Advanced Quantum Cascade Laser Transmitter Architectures and Infrared Photonics Development." In *SPIE Proceedings: Quantum Sensing and Nanophotonic Devices*, Vol. 5359, pp. 203-209. January 25, 2004, San Jose, California. eds: M Razeghi and GJ Brown. SPIE, Bellingham, Washington. Invited paper.

Sundaram SK, BR Johnson, MJ Schweiger, JE Martinez, BJ Riley, LV Saraf, JNC Anheier, PJ Allen and JF Schultz. 2004. "Chalcogenide Glasses and Structures for Quantum Sensing." In *SPIE Proceedings: Quantum Sensing and Nanophotonic Devices*, Vol. 5359, pp. 234-245. January 25, 2004, San Jose, California. eds: M Razeghi and GJ Brown. SPIE, Bellingham, Washington.

Johnson BR, MJ Schweiger and SK Sundaram. 2005. "Chalcogenide Nanowires by Evaporation-Condensation." *Journal of Non-Crystalline Solids* **351**(16-17):1410-1416.

Ho N, MC Phillips, A Qiao, PJ Allen, K Krishnaswami, BJ Riley, TL Myers and NC Anheier. 2006. "Single-Mode Low-Loss Chalcogenide Glass Waveguides for the Mid-Infrared." *Optic. Lett.* **31**(12):1860-1862.

Allen PJ, BR Johnson, RT Baran, JNC Anheier, SK Sundaram, MH Engelhard and BT Broocks. 2006. "Surface Degradation of As<sub>2</sub>S<sub>3</sub> Thin Films." *Phys. Chem. Glasses* **47**(6):681-687.

Riley BJ, BR Johnson, SK Sundaram, MH Engelhard, RE Williford and JD Olmstead. 2006. "Pressure-temperature Dependence of Nanowire Formation in the Arsenic-sulfur System." *Phys. Chem. Glasses* **47**(6):675-680.

Riley BJ, SK Sundaram, BR Johnson and LV Saraf. 2008. "Differential Etching of Chalcogenides for Infrared Photonic Waveguide Structures." *Journal of Non-Crystalline Solids* **354**(10-11):813-816.

Krishnaswami K, BE Bernacki, BD Cannon, MA Phillips, N Ho, PJ Allen and NC Anheier, Jr. 2007. "Beam Characteristics of Mid-IR Quantum Cascade Lasers." In *Quantum Electronics and Laser Science Conference, 2007. QELS '07*, pp. 1-2. May 6-11, 2007, Baltimore, Maryland. ed: B Bernacki. Optical Society of America.

Bernacki BE, K Krishnaswami, NC Anheier, Jr. and BD Cannon. 2008. "Design and Fabrication of Efficient Collimation and Focusing Optics for mid-IR Quantum Cascade Lasers." In *Laser Source Technology for Defense and Security IV* Vol. 6952, pp. 69520H-9. March 17, 2008, Orlando, Florida. eds: M Dubinskii and GL Wood. SPIE, Bellingham, Washington.

Bernacki BE, NC Anheier, K Krishnaswami, BD Cannon and KB Binkley. 2008. "Design and Fabrication of Efficient Miniature Retroreflectors for the Mid- and Long-Range Infrared." In *SPIE Proceedings: Infrared Technology and Applications XXXIV*, Vol. 6940, pp. 69400X-11, Orlando, Florida. eds: BF Andresen, GF Fulop and PR Norton. SPIE, Bellingham, Washington.

Krishnaswami K, BE Bernacki, BD Cannon, N Ho and NC Anheier, Jr. 2008. "Emission and Propagation Properties of Mid-Infrared Quantum Cascade Lasers." *IEEE Photon. Tech. Lett.* **20**(4):306-308.

Krishnaswami K, BE Bernacki, N Ho, PJ Allen and JNC Anheier. 2008. "Lateral Shearing Interferometer for Measuring Photoinduced Refractive Index Changes in Amorphous As<sub>2</sub>S<sub>3</sub>." *Rev. Sci. Instrum.* **79**(9):095101.

## **A.2 ITAS Photonics Project Conference Presentations**

Sundaram SK, BR Johnson, PJ Allen, NC Anheier, Jr., RM Williams and JF Schultz. 2002. "Laser Writing and Characterization of Structures in a Chalcogenide Glass." *Symposium KK: Femto and Attosecond Phenomena in Materials (Fall 2002 Program), MRS Fall Meeting*. December 1-6, 2002. Boston. Materials Research Society.

Sundaram SK, BR Johnson, MJ Schweiger, BJ Riley, JE Martinez, NC Anheier, PJ Allen, PL Gassman, CE Fay, R Dieken, BG Potter, HJ Barnaby, P Lucas and SA Macdonald. 2004. "Photo-modification of Chalcogenide Glasses." *2004 AAAS Annual Meeting*. February 2004. Seattle, Washington.

Schweiger MJ, SK Sundaram, NC Anheier, Jr., PJ Allen, BJ Riley, BR Johnson, JE Martinez and FW Liao. 2004. "Glass Formation and Laser Interactions Studies in Chalcogenide Systems." *American Ceramic Society Annual Meeting/Photonic Materials and Devices*. April 2004. Indianapolis, Indiana.

Sundaram SK, BR Johnson and NC Anheier, Jr. 2004. "Chalcogenide Glasses and Structures for Chemical Sensing." *Glass & Optical Materials Division Fall 2004 Meeting*. November 2004. Cocoa Beach, Florida.

Allen PJ, RT Baran, BR Johnson, MH Engelhard, BT Broocks and NC Anheier, Jr. 2004. "Surface Degradation of As<sub>40</sub>S<sub>60</sub> Thin Films." *Glass & Optical Materials Division Fall 2004 Meeting*. November 2004. Cocoa Beach, Florida.

Sundaram SK, PE Keller, BJ Riley, JE Martinez, BR Johnson, PJ Allen, LV Saraf, NC Anheier, Jr. and FW Liao. 2006. "Infrared Photonic Band Gap Materials and Structures." *Photonics West 2006*. San Jose, California.

Krishnaswami K, BE Bernacki, BD Cannon, MA Phillips, N Ho, PJ Allen and NC Anheier, Jr. 2007. "Beam Characteristics of Mid-IR Quantum Cascade Lasers." *Quantum Electronics and Laser Science Conference, 2007. QELS '07*, May 8, 2007, Baltimore, Maryland. Optical Society of America.

Anheier NC, Jr., BE Bernacki, K Krishnaswami and A Qiao. 2008. "Mid-Infrared Photonics Component Development Using Chalcogenide Glasses." *Glass & Optical Materials Division Meeting of the American Ceramic Society*. Tucson, Arizona.

Phillips MA, A Qiao, BE Bernacki and NC Anheier, Jr. 2008. "Characterization of Single-Mode Chalcogenide Glass Waveguides at 8.35  $\mu\text{m}$ ." *Conference on Lasers and Electro-Optics (CLEO)*. May 5-9, 2008. San Jose, California.

Qiao A, BR Johnson, JS McCloy, NA Carlie and NC Anheier, Jr. 2008. "Film Adhesion in Thick Chalcogenide Films." *8th Pacific Rim Conference on Ceramic and Glass Technology*. Vancouver, BC, Canada. Abstract submitted.

Qiao A, MA Phillips, BE Bernacki, NA Carlie, NC Anheier, Jr. and N Carlie. 2008. "Characterizing Chalcogenide Thin Film Waveguides at Mid-Infrared Wavelengths." *8th Pacific Rim Conference on Ceramic and Glass Technology*. Vancouver, BC, Canada. Abstract submitted.

Carlie NA, NC Anheier, Jr., A Qiao, MA Phillips, BE Bernacki, L Petit and K Richardson. 2008. "Measurement of the Refractive Index of Chalcogenide Thin Films Using Prism Coupling in the Near and Mid-Infrared." *8th Pacific Rim Conference on Ceramic and Glass Technology*. Vancouver, BC, Canada. Abstract submitted.

Bernacki BE, K Krishnaswami and NC Anheier, Jr. 2008. "Low Cost Plane Parallel Plate Lateral Shearing Interferometer for Infrared Laser Beam Diagnostics." *SPIE Defense Security and Sensing*. April 13-17, 2009. Orlando, Florida. Abstract submitted.

Krishnaswami K, A Qiao, BE Bernacki and NC Anheier, Jr. 2008. "Characterization of Single-mode Chalcogenide Fiber for Mid-Infrared Applications." *SPIE Defense Security and Sensing*. April 13-17, 2009. Orlando, Florida. Abstract submitted.

Anheier NC, Jr., BK Hatchell, KL Gervais, K Krishnaswami and BE Bernacki. 2008. "Compact Quantum Cascade Laser Transmitter." *SPIE Defense Security and Sensing*. April 13-17, 2009. Orlando, Florida. Abstract submitted.

### **A.3 ITAS Photonics Project Reports**

Anheier NC, Jr., PJ Allen, PE Keller, WD Bennett, PM Martin, BR Johnson, SK Sundaram, BJ Riley, JE Martinez, HA Qiao and JF Schultz. 2004. *FY 2004 Infrared Photonics Final Report*. PNNL-15209. Pacific Northwest National Laboratory, Richland, Washington.

Anheier NC, Jr., PJ Allen, N Ho, K Krishnaswami, BR Johnson, SK Sundaram, BJ Riley, JE Martinez, HA Qiao and JF Schultz. 2005. *FY 2005 Infrared Photonics Final Report*. PNNL-15581. Pacific Northwest National Laboratory, Richland, Washington.

Anheier NC, Jr., PJ Allen, BE Bernacki, N Ho, K Krishnaswami, HA Qiao and JF Schultz. 2006. *FY 2006 Infrared Photonics Final Report*. PNNL-16319. Pacific Northwest National Laboratory, Richland, Washington.

Anheier NC, Jr., BE Bernacki, BK Hatchell, N Ho, K Krishnaswami and HA Qiao. 2007. *FY 2007 Infrared Photonics Final Report*. PNNL-17392, Limited Distribution. Pacific Northwest National Laboratory, Richland, Washington.

Anheier NC, Jr., BE Bernacki, NA Carlie, KL Gervais, BK Hatchell, BR Johnson, K Krishnaswami, JS McCloy, MC Phillips and HA Qiao. 2008. *FY 2008 Infrared Photonics Final Report*. PNNL-XXXXX (in press). Pacific Northwest National Laboratory, Richland, Washington.

# Distribution

**No. of  
Copies**

- 1 Dr. Victoria T. Franques  
U.S. Department of Energy  
NNSA/NA-22  
1000 Independence Ave. SW  
Washington, DC 20585
- 1 Dr. Rhys M. Williams  
U.S. Department of Energy  
NNSA/NA-22  
1000 Independence Ave. SW  
Washington, DC 20585
- 1 Mr. Eric Sanders  
U.S. Department of Energy  
NNSA/NA-22  
1000 Independence Ave. SW  
Washington, DC 20585
- 1 Dr. Vaughn Standley  
U.S. Department of Energy  
NNSA/NA-22  
1000 Independence Ave. SW  
Washington, DC 20585

**No. of  
Copies**

- 18 **Internal Distribution**  
Pacific Northwest National Laboratory  
P.O. Box 999  
Richland, WA 99352
- Anheier, NC (3) K5-25  
Bernacki, BE K5-25  
Bruckner-Lea, C K5-25  
Clemmer, RG K8-02  
Dudder, GB K8-29  
Gervais, KL K5-22  
Hatchell, BK K5-22  
Johnson, BR K6-24  
Krishnaswami, K K5-25  
McCloy, JS K6-24  
Myers, TL K5-25  
Phillips, MC K5-25  
Sharpe, SW K8-88  
Qiao, HA K5-20  
Information Release Office (2) K1-06



**Pacific Northwest**  
NATIONAL LABORATORY

902 Battelle Boulevard  
P.O. Box 999  
Richland, WA 99352  
1-888-375-PNNL (7665)

[www.pnl.gov](http://www.pnl.gov)



U.S. DEPARTMENT OF  
**ENERGY**